Physics of Fluids

Stability of flow in a deformable channel with an unrestrained boundary

Shraddha Mandloi[1] and V. Shankar[1, a)]
Department of Chemical Engineering, Indian Institute of Technology, Kanpur 208016, India

(Dated: 8 May 2020)

We report results from a linear stability analysis of Newtonian plane Poiseuille flow through a deformable linear elastic channel with an unrestrained boundary wherein the deformable wall is not rigidly bonded to a substrate, and is free to undergo motion. The objective of this study is to address the experimental observations of instabilities for this configuration (S. S. Srinivas and V. Kumaran, J. Fluid Mech., **822**, 267-306, 2017). We analyze the role of an unrestrained deformable boundary on the stability of channel flow using both asymptotic and numerical methods. Our results show that, when solid to fluid layer thickness ratio is $O(1)$, both wall modes (whose critical Reynolds number, $Re_c \propto G^{3/4}$; G being the shear modulus of the solid) and inviscid modes (whose $Re_c \propto G^{1/2}$) are significantly destabilized by the presence of an unrestrained boundary when compared to channels with completely bonded deformable boundaries. In agreement with experimental observations, the eigenfunctions corresponding to both these unstable modes exhibit a pronounced asymmetric behaviour, thereby highlighting the influence of the unrestrained deformable boundary on the stability of the flow. The asymptotic predictions for the wall mode instability are shown to be in excellent agreement with our numerical results. However, for solid to fliud thickness ratio ~ 7.7 (used in the aforementioned experiments), our results show that the reduction in the critical Reynolds number due to the unrestrained boundary is only moderate; we provide possible reasons for the same.

[a)]Author for correspondence; E-mail: vshankar@iitk.ac.in

I. INTRODUCTION

Flow past deformable surfaces has been studied extensively in the past few decades since Kramer[1,2] explored the possibility of using compliant coatings to delay the transition to turbulence in boundary-layer flows in the early 1960's. However, the study of internal flow through deformable tubes and channels has gained attraction in the mid-1970's[7,8] due to its relevance to flow of biological fluids in deformable conduits, such as the flow of blood in blood vessels[30], the flow of air in the respiratory system[36]. More recently, advancements in the field of microfluidics[32] and availability of polymer-based materials (such as polydimethyl siloxane, abbreviated PDMS)[26] have demonstrated the use of soft deformable surfaces for the fabrication of lab-on-chip devices[29], organ-on-chip devices[34], and robotic actuators[46] that are controlled using flow in soft microchannels. Thus, it has now become possible to address the fundamental issue of mixing in microconduits made of soft elastomers, by employing passive manipulation techniques that rely on altering the wall-elasticity to induce hydrodynamic instabilities that occur due to the dynamical coupling between flow and deformation. This coupling is shown to result in a transition to a new type of turbulence in flow past deformable solid surfaces[20,33,35,38,39,41,43].

The theoretical study of flow past deformable surfaces was initiated by Benjamin[3,5] and Landhal[4] who examined the effect of compliant surfaces on the stability of the flow. Benjamin extended the classical theory of Tollmien and Schlichting[9] to deformable surfaces and suggested that the Tollmien-Schlichting instability (TSI) is suppressed by the presence of a flexible, non-dissipative wall; however, the presence of damping in the flexible surface destabilises the TSI. Benjamin[3] and Landhal[4] also introduced new classes of modes for flow past deformable surfaces that are absent in flow past rigid surfaces termed as 'flow-induced surface instabilities' (FISI). Many subsequent efforts[6,10,11,13,16] focused on the study of the modification of TSI by the introduction of flexible walls, modeled as spring-backed plates that undergo purely normal motion, and concluded that the presence of a flexible wall has a stabilising effect on the TSI. These studies were motivated by the experiments of Kramer[1,2] and by the applications in marine and aerospace industries, and hence focused on the stability of the flow in the high-Reynolds number regime. However, the experiments of Lahav *et al.*,[7] Krindel and Silberberg[8] on gel-coated tubes showed the transition to turbulence in a gel coated tube occurs at Reynolds number lower than 2000, and thereby stimulated many theoretical and numerical studies of the stability of internal flows through deformable conduits, in the low to moderately high Reynolds number regime as well.

Kumaran, Fredrickson, and Pincus[14] first analyzed the linear stability of plane Couette flow past a deformable wall modeled as a linear viscoelastic solid[12], i.e., a continuum model that accounts for both the elastic and dissipative nature of the deformable solid, in the absence of inertial effects in the fluid and solid. They showed that flow instabilities in such systems occur due to the transfer of energy from mean flow to the perturbations that in turn destabilises the solid-fluid interface. These theoretical predictions are in quantitative agreement with the experiments performed by Kumaran and Muralikrishnan[20]. The theoretical study by Kumaran *et al.*[14] was further extended to high Reynolds number by Srivatsan and Kumaran[17] that indicates the presence of wall mode instability ($Re \sim G^{3/4}$) in the high Reynolds number limit where G is the shear modulus of the deformable solid. The wall-mode instabilities are characterized by the presence of the wall layer of thickness $O(Re^{-1/3})$ smaller than the channel width or tube diameter, such that the viscous stresses in the fluid layer become comparable to the inertial stresses. Also, a delicate balance between the viscous stresses in the wall layer and elastic stresses in the deformable wall is present for this class of instabilities. Later, Shankar and Kumaran[25,27] performed an asymptotic analysis in the high Reynolds number limit and showed that tangential wall motion is a crucial requirement to realize

the wall mode instability, and hence it is expected to be present for flexible walls modeled using viscoelastic continuum models. They also established the fact that the gradient of the velocity for the base flow profile at the wall has a significant influence on the wall-mode instability, although it remains unaffected by the detailed variation of the base state flow velocity profile. Another type of instability that is predicted in the high Reynolds number limit is termed as the "inviscid instability" ($Re \sim G^{1/2}$) as the viscous forces in the fluid are usually insignificant in comparison to the inertial forces in this limit except in a wall layer of thickness $O(Re^{-1/2})$ near the deformable wall and a "critical layer" of thickness $O(Re^{-1/3})$. This instability is characterized by the balance between the inertial stresses in the fluid and elastic stresses in the deformable solid ($\rho V^2/G \sim 1$)[15,22] and the presence of a critical layer near the point of singularity, where the base flow velocity equals the wavespeed of the disturbance[9,21,42].

Gkanis and Kumar[28,31] suggested employing a nonlinear and material frame-invariant neo-Hookean model for the deformable solid layer, in lieu of the linear elastic model, that is consistent with finite base-state deformations. They showed the presence of a short-wave instability that is absent for linear viscoelastic solid in the creeping-flow limit for plane Poisuielle flow. This work was further extended to a wider range of Reynolds numbers by Gaurav and Shankar[35]. They predicted a new class of long-wavelength unstable modes along with short-wave instabilities by introducing consistent boundary conditions at a solid-fluid interface. However, for the high Reynolds number regime, incorporation of the neo-Hookean model does not have a significant effect on the stability of the most unstable modes. A detailed summary of the theoretical studies for the flow past deformable surfaces can be found in Refs. 21 and 42. Recently, Patne *et al.*[44,47] proposed a consistent L3 neo-Hookean solid model to remove the disparities in the various formulations used for the description of the neo-Hookean solid. While the low-Reynolds number instability predicted by Gaurav and Shankar[35] ceases to exist for the new consistent formulation, the results in the high Reynolds number limit matches with their results for the neo-Hookean solid, and with the predictions obtained using the linear-viscoelastic model. Thus, a simpler linear-viscoelastic solid model can be used to predict the stability of wall and inviscid modes in the high Reynolds number regime, the regime of focus in this study.

While the effect of a deformable solid wall on the stability of the flow in the low Reynolds number regime has been experimentally established[20], recently, Verma and Kumaran[38] performed experiments for plane Poiseuille flow in the high Reynolds number regime in channels made of PDMS gel and observed transition to the turbulence at much lower Reynolds number ($Re \sim 500$) compared to the transition in rigid channels ($Re \sim 1200$). Also, they showed that the experimentally obtained transition Reynolds number is about an order of magnitude lower than the theoretically predicted transition Reynolds number for wall modes and it scales as $\Sigma^{5/8}$ (where $\Sigma = (\rho G R^2)/(\eta^2)$ is a nondimensional parameter that depends on the fluid and solid properties), where the exponent $5/8$ is in between the theoretical prediction for wall modes ($3/4$) and inviscid modes ($1/2$). Later, Verma and Kumaran[39] argued that this discrepancy arises because the pressure gradient deforms the soft solid to the extent that it modifies the laminar velocity profiles and the pressure gradients in laminar flow. This subsequently alters the transition Reynolds number and scaling in experiments. When the altered laminar velocity profile due to the deformation in the channel is accounted for in the linear stability analysis, they showed that the experimental observations agree with the theoretical predictions. Srinivas and Kumaran[45] probed higher values of Σ in their experiments by analyzing the flow of a Newtonian fluid in a deformable channel made of polyacrylamide (PAA) gel with an unrestrained top boundary. They showed that flow undergoes two types of transition, namely, "soft wall transition" that has characteristics similar to the flow transitions observed by Kumaran and co-workers[37,39,40,43] and "wall flutter transition" that

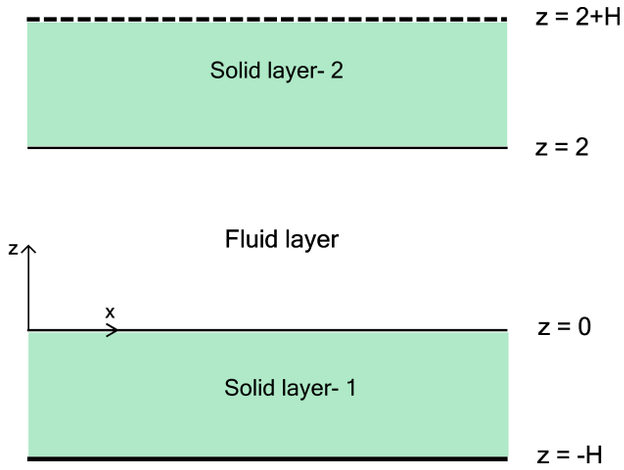

FIG. 1: Schematic diagram showing the configuration and the non-dimensionalised coordinate system under consideration. The unrestrained solid boundary at $z = 2 + H$ is represented by dashed line, while the solid line at $z = -H$ represent the solid layer strongly bonded to a rigid substrate.

occurs after the soft wall transition is observed for the flow and is present only for the unrestrained boundary. This transition is characterised by asymmetric velocity fluctuations that are higher near the unrestrained boundary and by downstream traveling waves on the surface of the unrestrained wall. The transition Reynolds numbers for wall flutter transition scales as $\Sigma^{1/2}$ that is similar to the theoretically predicted scaling for inviscid instability for the internal flows[15,18,35] and the wall flutter instabilities for the external flows[3–5].

However, the effect of an unrestrained, deformable boundary on flow instabilities has not been addressed hitherto from a theoretical stand point. Thus, in this work, we analyze the stability of pressure-driven flow of a Newtonian fluid through a deformable channel modeled as a linear-elastic solid with an unrestrained top boundary to understand the influence of this boundary condition on the flow instabilities encountered at higher Reynolds numbers in internal flows. We restrict our analysis to 2D disturbances for the following reason. The experiments performed by Srinivas and Kumaran[45] used channels with a relatively large aspect ratio W/R ratio of ~ 15 and ~ 43, where W is the width of the channel, and R represents the half-height of the channel. Thus, the 2D flow approximation (corresponding to an infinite aspect ratio) used in our stability analysis is expected to be sufficient to describe these experiments. The experiments report asymmetrical fluctuations for the wall-flutter transition that is exclusively observed for an unrestrained deformable boundary. We observe a similar impact of the unrestrained deformable boundary in our theoretical analysis of the system that is supported with the help of eigenfunctions in figures 9-14. These similarities of the theoretical predictions with the experiments show that the solid model and linear stability analysis accurately capture the complicated dynamics of the system. This has now been clarified in page ?? of the revised manuscript.

The rest of this paper is structured as follows: In section II we present the governing equations for plane-Poiseuille flow along with the boundary conditions, base state solutions and the details of the linear stability analysis. In section III, we discuss the results obtained using numerical and asymptotic methods and present the major conclusions of the study in section IV. The details of the asymptotic analysis performed for the wall mode instability are provided in the Appendix.

II. PROBLEM FORMULATION

We consider the pressure-driven flow of an incompressible Newtonian fluid through a rectangular channel lined with a deformable solid, as shown in figure 1. The fluid of density ρ and viscosity η flows in the region $0 < z^* < 2R$, through the deformable solid layers of thickness HR which occupies the region $-HR < z^* < 0$ and $2R < z^* < (H+2)R$, where, the superscript asterisk (*) is used to represent the dimensional quantities. The impermeable and incompressible solid layers are modeled as a linear elastic solid of density ρ_s, and the coefficient of elasticity G and the ratio of the densities of solid and fluid are considered to be unity. We further consider that the lower solid layer is strongly bonded to a rigid and impermeable surface at $z^* = -HR$ and the upper solid layer is in contact with a passive gas at an unperturbed gas-solid interface at $z^* = (H+2)R$.

We have used the following scheme to non-dimensionalize the dynamic quantities: Lengths are scaled by the half-width of the fluid layer R, velocities are scaled by $(G/\rho)^{1/2}$, pressure and stresses are scaled by the shear modulus of the solid G. Under steady-state conditions, we consider the flow of the Newtonian fluid to be unidirectional and fully developed, and the non-dimensional velocity fields in the liquid layer are given by:

$$\bar{v}_x(z) = \Gamma(2z - z^2)\,, \tag{1}$$

$$\bar{v}_z = 0\,. \tag{2}$$

Here, $\Gamma = (\rho V_{max}^2/G)^{1/2}$, is the non-dimensional maximum velocity in the fluid, and V_{max} is the maximum dimensional velocity of the fluid under the laminar flow conditions.
The non-dimensional mass and momentum balance equations for the fluid take the following form:

$$\partial_i v_i = 0\,, \tag{3}$$

$$\left[\partial_t + v_j\partial_j\right] v_i = -\partial_i p_f + \frac{\Gamma}{Re}\partial_j \tau_{ij}\,, \tag{4}$$

where, $\partial_t = \partial/\partial t$ and v_i represents the velocity flow field. The indices i, j can take on the values x, z representing the directions in the Cartesian plane. The Reynolds number used in equation (4) is defined as $Re = \rho V_{max} R/\mu$. The total stress tensor in the liquid layer can be written as $T_{\text{ij}} = -p_f\,\delta_{\text{ij}} + \tau_{\text{ij}}$, where p_f is the isotropic pressure, $\tau_{\text{ij}} = \frac{\Gamma}{Re}\left(\partial_i v_j + \partial_j v_i\right)$ is the non-dimensional deviatoric stress tensor for the Newtonian fluid.
The deformable solid layer is modeled using the linear elastic constitutive relation which leads to the following non-dimensionalised governing equations:

$$\partial_i u_i = 0\,, \tag{5}$$

$$\partial_t^2 u_i = \partial_j \Pi_{ij}\,. \tag{6}$$

Here, u_i represents the displacement field in the solid, defined as the deviation of material points from their initial positions when a stress is applied on the solid. Hence, the velocity field in the solid layer is given as $v_i = \partial_t u_i$. The total stress tensor in the solid layer Π_{ij}, is given as $\Pi_{\text{ij}} = -p_s\,\delta_{\text{ij}} + \sigma_{\text{ij}}$, where p_s is the isotropic pressure, and $\sigma_{\text{ij}} = (\partial_i u_j + \partial_j u_i)$ is the deviatoric elastic stress tensor. The above set of equations is solved using the following boundary conditions. We use zero-displacement boundary conditions at $z = (-H)$ as the solid layer is assumed to be perfectly bonded to a rigid, impermeable plane. At the liquid-solid interfaces in the system at $(z = 0)$ and $(z = 2)$, boundary conditions for the continuity of normal and tangential velocities as well as stresses are applied and at the free surface, i.e. $z = H + 2$, boundary conditions for the continuity of normal and tangential stresses are applied to define the system completely.

A. Linear stability analysis

A temporal linear stability analysis is performed on the coupled fluid-solid system by imposing small perturbations (denoted by primed quantities) about the base states (denoted by overbars). All the dynamic variables in the fluid layer, as well as the solid layer, are perturbed as $\phi = \bar{\phi} + \phi^{'}$, and the perturbed quantities are further expanded in the form of Fourier modes in the x-direction, with an exponential dependence in time:

$$\phi^{'}(x,z,t) = \tilde{\phi}(z)\exp[ik(x-ct)]\,. \tag{7}$$

Here, k is the wavenumber that is inversely proportional to the wavelength of perturbations, c is the complex wavespeed, given as $c = c_r + ic_i$, that determines the growth of perturbations. If the imaginary part of the wavespeed, $c_i > 0$, the perturbations imposed onto the base state will grow with time, and the system will be temporally unstable. Here, $\tilde{\phi}(z)$ represents the eigenfunctions which can be obtained by solving the linearised governing equations determining the stability of the system. As two-dimensional perturbations are shown to be more unstable than three-dimensional perturbations by Patne and Shankar[47] for the flow of Newtonian fluid in deformable channel modeled using the neo-Hookean model, we impose two-dimensional perturbations (neglecting the variations in the y-direction) to analyse the stability of the system.
The equations governing the dynamics of the fluid (3)-(6) are linearised by perturbing the dynamical variables and retaining the terms linear in perturbation variables. The linearised governing equations for the fluid take the following form after substitution of the Fourier mode expansions (7) in the perturbation variables:

$$d_z\tilde{v}_z + ik\tilde{v}_x = 0\,, \tag{8}$$

$$[ik(\bar{v}_x - c)\tilde{v}_x + (d_z\bar{v}_x)\tilde{v}_z] = -ik\tilde{p} + \frac{\Gamma}{Re}(d_z^2 - k^2)\tilde{v}_x\,, \tag{9}$$

$$[ik(\bar{v}_x - c)\tilde{v}_z] = -d_z\tilde{p} + \frac{\Gamma}{Re}(d_z^2 - k^2)\tilde{v}_z\,. \tag{10}$$

The linearized governing equations for the displacement field in the solid layers are as follows:

$$d_z\tilde{u}_{zi} + ik\tilde{u}_{xi} = 0\,, \tag{11}$$

$$k^2c^2\tilde{u}_{xi} - ik\tilde{p}_s + (d_z^2 - k^2)\tilde{u}_{xi} = 0\,, \tag{12}$$

$$k^2c^2\tilde{u}_{zi} - d_z\tilde{p}_s + (d_z^2 - k^2)\tilde{u}_{zi} = 0\,, \tag{13}$$

where i takes the values 1 and 2 representing solid layers 1 and 2 respectively.
These linearised equations are solved together with the linearised boundary conditions mentioned below. The zero-displacement conditions imposed at $z = -H$ are:

$$\tilde{u}_{z1} = 0\,, \tag{14}$$

$$\tilde{u}_{x1} = 0\,. \tag{15}$$

At the solid-fluid interface, boundary conditions for continuity of velocity and stresses are applied by Taylor expanding the mean flow and perturbed variables about the unperturbed interface at $z = 0$. The terms linear in perturbation variables are retained to obtain the following conditions:

$$\tilde{v}_z = -ikc\tilde{u}_{z1}\,, \tag{16}$$

$$\tilde{v}_x + d_z\bar{v}_x|_{z=0}\,\tilde{u}_{z1} = -ikc\tilde{u}_{x1}\,, \tag{17}$$

$$Re^{-1}\Gamma(d_z\tilde{v}_x + ik\tilde{v}_z) = d_z\tilde{u}_{x1} + ik\tilde{u}_{z1}\,, \tag{18}$$

$$-\tilde{p}_f + 2Re^{-1}\Gamma d_z\tilde{v}_z = -\tilde{p}_{s1} + 2d_z\tilde{u}_{z1}\,. \tag{19}$$

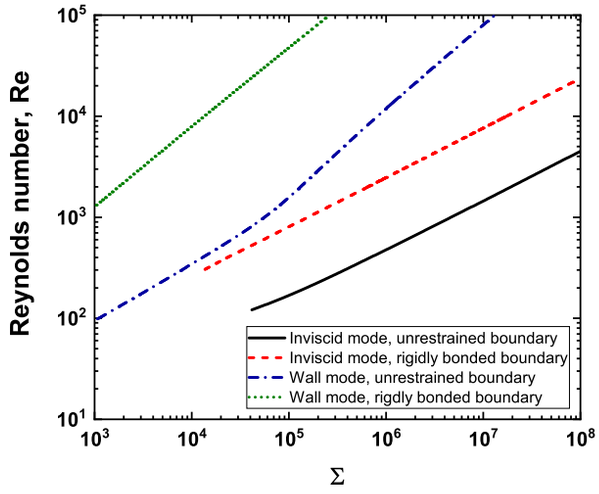

FIG. 2: Neutral stability curves in Re-Σ plane for rigidly bonded and unrestrained boundary conditions at $z = H + 2$: Data for $H = 1$ and $k = 1$.

Here, the equations (16) and (17) represent normal and tangential continuity conditions for the velocity field and the equations (18) and (19) represent normal and tangential continuity of stresses. We obtain similar conditions for the fluid-solid interface at $z = 2$:

$$\tilde{v}_z = -ikc\tilde{u}_{z2}\,, \tag{20}$$

$$\tilde{v}_x + d_z\bar{v}_x|_{z=2}\,\tilde{u}_{z2} = -ikc\tilde{u}_{x2}\,, \tag{21}$$

$$Re^{-1}\Gamma(d_z\tilde{v}_x + ik\tilde{v}_z) = d_z\tilde{u}_{x2} + ik\tilde{u}_{z2}\,, \tag{22}$$

$$-\tilde{p}_f + 2Re^{-1}\Gamma d_z\tilde{v}_z = -\tilde{p}_{s2} + 2d_z\tilde{u}_{z2}\,. \tag{23}$$

At $z = H + 2$, we consider the solid layer is exposed to a passive gas and hence it experiences no tangential as well as normal stress at the gas-solid interface. The linearised boundary conditions are as follows:

$$d_z\tilde{u}_{x2} + ik\tilde{u}_{z2} = 0\,, \tag{24}$$

$$-\tilde{p}_{s2} + 2d_z\tilde{u}_{z2} = 0\,. \tag{25}$$

The above two boundary conditions (Eq. 24-25) represent a significant departure from all the earlier studies in this area by considering an unrestrained or unbonded solid boundary.

The linearised governing equations (8)-(13) along with the boundary conditions (14)-(25) constitute a differential eigenvalue problem that is numerically solved using the spectral collocation method.[19,23] The linearised governing equations are represented in a generalised eigenvalue problem of form $c^2\mathbf{Ax} + \mathbf{cBx} + \mathbf{Cx} = \mathbf{0}$, where the complex wavespeed c (function of Re, k, H, Γ) is the eigenvalue, $\mathbf{A}, \mathbf{B}$ and $\mathbf{C}$ are the coefficient matrices and the column vector $\mathbf{x}$ contains the eigenvectors. The validity of the eigenvalues obtained using the spectral method is checked using the shooting method with ortho-normalization[35]. The agreement between the eigenvalues obtained using shooting and spectral methods is between 6 to 8 decimal places.

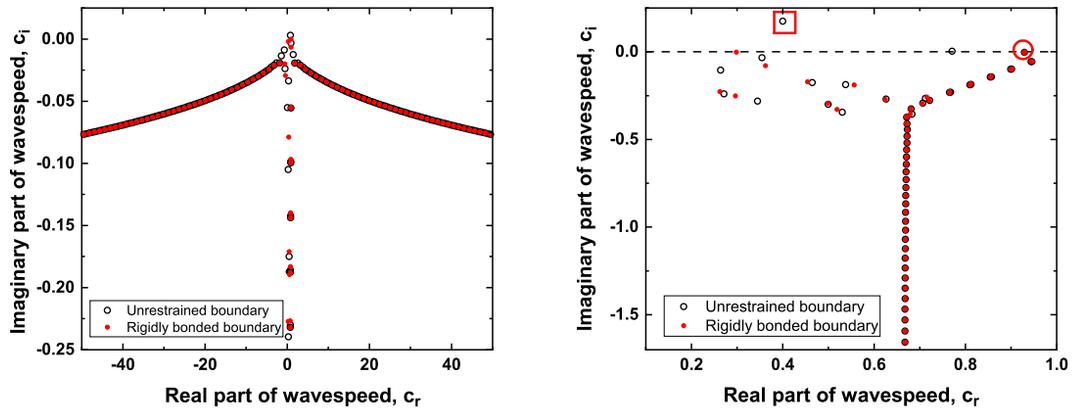

(a) Full eigenvalue spectrum

(b) Enlarged spectrum

FIG. 3: Eigenvalue spectrum showing the effect of unrestrained boundary. Data for $H = 1$, $k = 1$, $Re = 4000$ and $\Gamma = 2.4398$. Panel (a) shows the overall picture, while Panel (b) shows the enlarged region near the A, P, S branches.

III. RESULTS AND DISCUSSION

In this section, we present results from linear stability analysis of pressure-driven flow of a Newtonian fluid in a deformable channel with an unrestrained boundary at $z = H+2$ to understand its effect on the flow in the high Reynolds number regime. In figure 2, we present a neutral stability curve ($c_i = 0$) in the Re-Σ plane, for $H = 1$ and $k = 1$, to compare the effects of the unrestrained boundary at $z = H + 2$, with a similar system that considers the deformable solid layer-2 to be perfectly bonded to a rigid surface at $z = H + 2$ (henceforth referred as 'rigidly bonded' boundary condition) and satisfies the boundary conditions $\tilde{u}_{x2} = 0$ and $\tilde{u}_{z2} = 0$. We observe that in the high-Re limit, two distinct modes, namely, wall modes ($Re \propto \Sigma^{3/4}$) and inviscid modes ($Re \propto \Sigma^{1/2}$) exist for the present system where, $\Sigma = \rho G R^2/\eta^2 = (Re/\Gamma)^2$, is a non-dimensional parameter that is independent of fluid velocity and is a function of fluid and deformable wall properties.

We find that for wall modes, the presence of an unrestrained top boundary reduces the threshold Re for instability by an order of magnitude, i.e., for $\Sigma = 1 \times 10^5$, the transition Reynolds number for the rigidly-bonded boundary condition at $z = H + 2$ is $\sim 5 \times 10^4$, whereas the transition Reynolds number for the system with unrestrained top boundary is ~ 1650. In a similar manner, the inviscid mode is also significantly destabilised by the presence of the unrestrained boundary. In figures 3a and 3b, we show the eigenvalue spectrum for both rigidly-bonded and unrestrained boundary conditions at $z = H+2$, for $H = 1$ and $k = 1$. We have fixed the value of the parameter Γ such that there is a neutrally stable mode for the rigidly-bonded boundary condition (marked by a red circle, in figure 3b). For the unrestrained boundary condition, at the same value of Γ, we observe that the neutrally stable mode (present for the rigidly-bonded boundary) destabilises marginally. However, a new mode (marked by a red square) evolves from the series of eigenvalues near $c_i = 0$ present due to the wall layer that destabilises the flow. Also, the eigenvalues present on the A, P, S branches[24] are observed to be only marginally altered by the presence of the unrestrained boundary at $z = H + 2$ for the given set of parameters.

The substantial reduction in the threshold Re for instability due to the unrestrained boundary prompted us to further investigate its effects for the higher values of H, used in the experiments

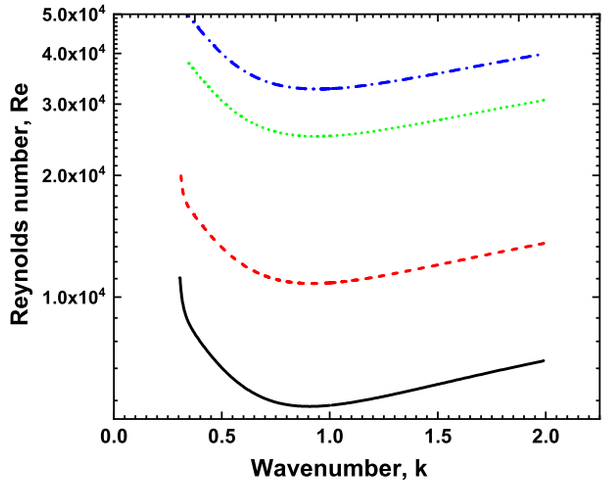

FIG. 4: Neutral stability curves in the Re-k plane for the wall mode for $H = 7.77$.The solid line (—) represent $\Sigma = 1.01 \times 10^6$, dashed line (- - -) represent $\Sigma = 2.42 \times 10^6$, dotted line (····) represent $\Sigma = 7.47 \times 10^6$ and dashed-dotted line (-·-) represent $\Sigma = 1.02 \times 10^7$.

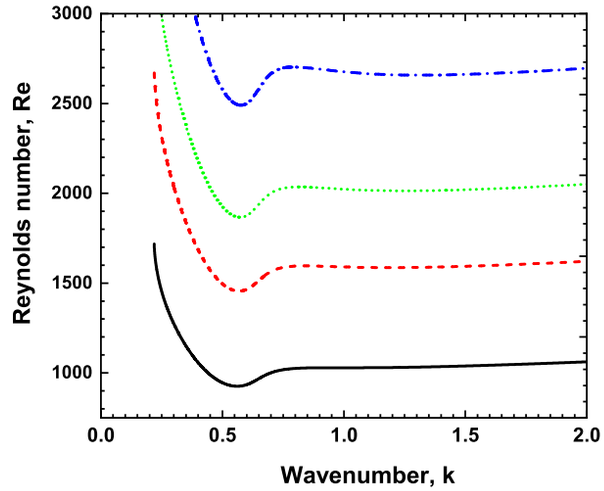

FIG. 5: Neutral stability curves in the Re-k plane for the inviscid mode for $H = 7.77$. The solid line (—) represent $\Sigma = 1.01 \times 10^6$, dashed line (- - -) represent $\Sigma = 2.43 \times 10^6$, dotted line (····) represent $\Sigma = 4.03 \times 10^6$ and dashed-dotted line (-·-) represent $\Sigma = 7.11 \times 10^6$.

by Srinivas and Kumaran[45]. In figure 4, we present Re vs k curves for wall modes at $H = 7.7$ for fixed values of the parameter Σ to obtain the minimum value of the Reynolds number (Re_{cr}) with variation in the wavenumber, k. The value of k for which Re is minimum is termed as the critical wavenumber, k_{cr}. A similar procedure is repeated to obtain the critical wavenumbers for the inviscid mode for the fixed values of the parameter Σ, as shown in figure 5.

In figure 6, we present neutral stability curves showing the variation of critical Reynolds number with Σ at critical wavenumbers (k_{cr}) for wall modes and inviscid modes at $H = 7.77$. We observe that both the modes are destabilised by the presence of the unrestrained boundary at

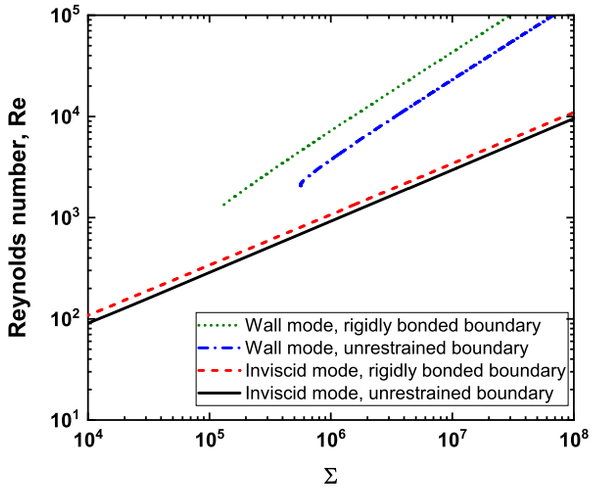

FIG. 6: Comparison of neutral stability curves in Re-Σ plane for different configurations (rigidly bonded and unrestrained boundary conditions at $z = H + 2$): Data for $H = 7.77$ and $k = k_{cr}$.

$z = H + 2$. However, the reduction in Re_c due to the unrestrained boundary is not as drastic it was for $H = 1$. Also, for a fixed value of the parameter Σ, the difference in the critical Reynolds number for the wall mode is more as compared to the inviscid mode, indicating that the presence of the unrestrained boundary has a higher impact on the stability of wall modes for higher values of H. When compared with the experiments of Srinivas and Kumaran[45] at $\Sigma = 2.43 \times 10^6$ and $\Sigma = 7.10 \times 10^6$ (the values of Σ at which experiments observe an instability for $H = 7.77$) the theoretically predicted values for the critical Reynolds number ($Re_{cr} \sim 7690$ for $\Sigma = 2.43 \times 10^6$ and $Re_{cr} \sim 15000$ for $\Sigma = 7.10 \times 10^6$) for soft wall transition (experimental equivalent for wall mode instability) is an order of magnitude higher than the experimentally observed transition Reynolds number ($Re \sim 1430$ for $\Sigma = 2.43 \times 10^6$ and $Re \sim 1882$ for $\Sigma = 7.10 \times 10^6$). This disparity is similar to the one addressed by Verma and Kumaran[38,39], and, in principle, ought to be resolved by the inclusion of the change in the shape of the deformable wall with the flow and the concomitant change in the base-state velocity profile. The theoretically predicted critical Reynolds number ($Re_{cr} \sim 1300$ for $\Sigma = 2.43 \times 10^6$ and $Re_{cr} \sim 2250$ for $\Sigma = 7.10 \times 10^6$) is observed to be in close proximity of experimentally captured transition Reynolds number ($Re \sim 1790$ for $\Sigma = 2.43 \times 10^6$ and $Re \sim 2410$ for $\Sigma = 7.10 \times 10^6$) for the wall flutter transition ($\Sigma \sim Re^{1/2}$); however, the effect of the unrestrained boundary is not significant for this mode of instability.

We also performed an asymptotic analysis for the wall modes by following the procedure of Shankar and Kumaran[27] to understand the effect of the unrestrained boundary condition on the wall modes, and the details of this analysis are discussed in Appendix. As shown in figure 7, for $H = 7.77$ and $k = k_{cr}$, the results obtained from the asymptotic analysis are in good agreement with the complete numerical solution of the governing equations at high Reynolds number for both the rigidly bounded boundary condition and the unrestrained boundary condition at $z = H + 2$. The relative error in the dimensionless maximum velocity ($|\Gamma_{numerical} - \Gamma_{asymptotic}|/\Gamma_{numerical}$) and the leading order wavespeed ($|c_{numerical} - c^{(0)}|/c_{numerical}$), obtained using the numerical and the asymptotic solutions to the governing equations, are plotted against the Reynolds number in figure 8, that shows that the relative error in Γ_0 and the leading order wavespeed $c^{(0)}$ decreases as $Re^{-1/3}$, as per the prediction of the asymptotic analysis.

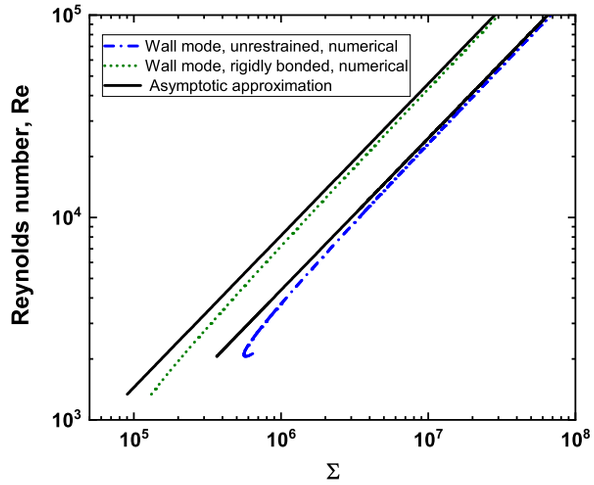

FIG. 7: Neutral stability curves in Re-Σ plane for different configurations (rigidly bonded and unrestrained boundary conditions at $z = H + 2$) comparing the asymptotic results with numerical results for the wall modes: Data for $H = 7.77$ and $k = k_{cr}$.

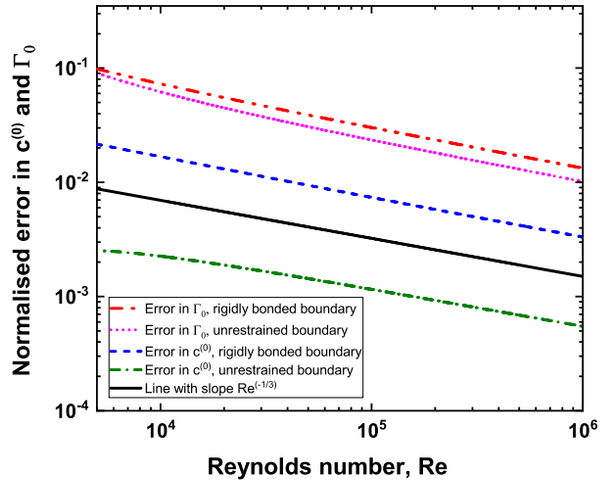

FIG. 8: Variation of relative error in leading order wavespeed ($c^{(0)}$) and non-dimensional maximum velocity (Γ) for different configurations (rigidly bonded and unrestrained boundary conditions at $z = H + 2$): Data for $H = 7.77$ and $k = k_{cr}$.

Figures 9a and 9b show the variation of real and imaginary parts of the eigenfunction $\tilde{v}_x$ (normalised by the maximum velocity) with z for the wall modes at $H = 7.77$ and k_{cr}. We note that the velocities are very large near the fluid-solid interface at $z = 2$, i.e., the fluid-solid interface near the unrestrained boundary at $z = H + 2$ in contrast to the little variation at $z = 0$, the fluid-solid interface for solid layer-1, that is perfectly bonded to a rigid substrate at $z = -H$. This suggests that the dynamics of the system is dominated by the deformable solid layer near the unrestrained boundary. Also, with an increase in the Reynolds number, the boundary layer thickness decreases,

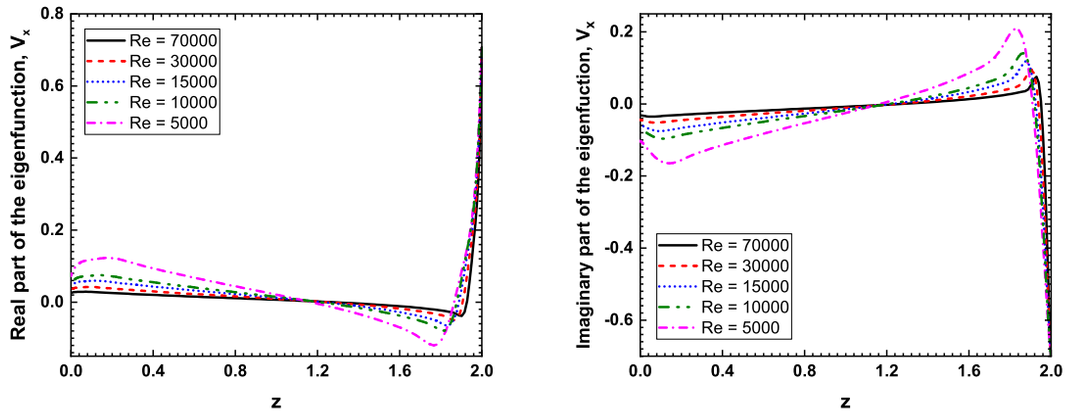

(a) Re[$\tilde{v}_x$] (b) Im[$\tilde{v}_x$]

FIG. 9: Normalised eigenfunction $\tilde{v}_x$ for the most unstable wall-mode at different Reynolds number. Panel (a) show the real part of the eigenfunction $\tilde{v}_x$ and Panel (b) show the imaginary part of the eigenfunction $\tilde{v}_x$ for $H = 7.77$, $k_{cr} = 0.92$ and Re as shown in figure.

which suggests an inverse proportionality with Reynolds number that is further verified by the asymptotic analysis. In a similar manner, a sharp transition in the velocity is observed for the eigenfunction $\tilde{v}_z$ near the fluid-solid interface at $z = 2$, as shown in figures 10a and 10b. The presence of an unrestrained (free) boundary increases the perturbations at the fluid-solid interface near the unrestrained boundary ($z = 2$), as illustrated by the eigenfunctions ($\tilde{v}_x, \tilde{v}_z$), thereby making the flow more unstable. If we allow the outer boundaries of both the walls to move freely, the system is expected to destabilize further. In such a configuration, the eigenfunctions for both the wall and inviscid modes can either be symmetric or antisymmetric about the channel center, representing 'varicose' or 'sinuous' modes of wall deformations. That possibility is precluded by the presence of one rigidly-bonded boundary in the present study.

The eigenfunctions obtained for the inviscid mode for $H = 7.77$ and k_{cr} are shown in figures 11 and 12. For the variation of the tangential velocity fluctuation $\tilde{v}_x$ with z, we observed the following: first, the eigenfunctions do not vary significantly over an extensive range of Reynolds number, indicating that the dynamics of the inviscid mode is independent of the Reynolds number in most of the region. Second, it can be observed that there is a sharp change in the slope of the eigenfunctions near $z = 2$, i.e., the fluid-solid interface near the unrestricted boundary, that also gets steeper with the increase in the Reynolds number (as shown in the inset of the figure 11), indicating the presence of a boundary layer near $z = 2$. Third, the eigenfunction has a constant value (~ 0) in the domain 0 to 1, i.e., there is no effect of the solid layer-1 (perfectly bounded to a rigid surface at $z = -H$), on the inviscid dynamics of the system and fourth, a slight variation is observed in the eigenfunctions with the Reynolds number, at $z = 1$, i.e., the centerline of the channel indicating that a boundary layer can be present there that alters the behavior of the eigenfunctions in the $z = 0$ to $z = 1$ region. All these observations imply that the presence of the unrestrained boundary ultimately dictates the dynamics of the system for both wall and inviscid modes. It is noted here that the asymmetric behavior in the normal and tangential velocity fluctuations (v'_x, v'_z) was observed for the wall flutter transition in the experimental study by Srinivas and Kumaran[45] where they show that the fluid velocity fluctuations near the unrestrained wall are higher than the fluctuations near the deformable wall rigidly bonded to a solid substrate, for the flow a Newtonian

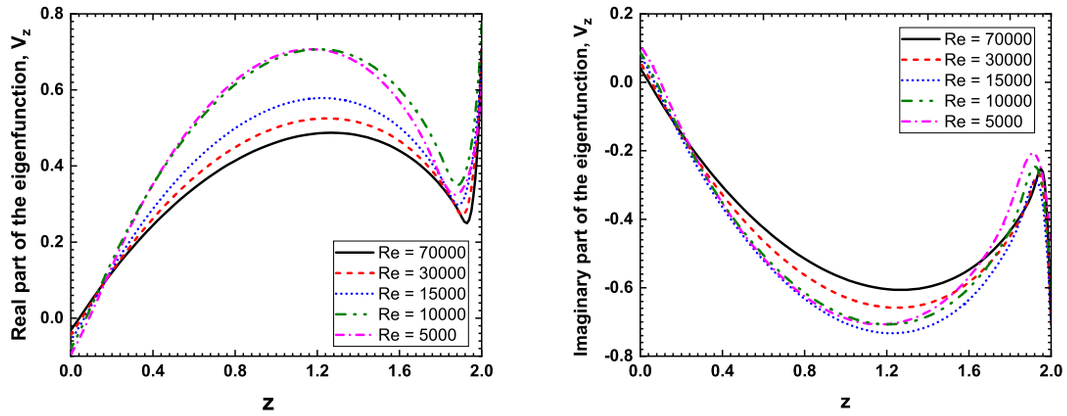

(a) Re[$\tilde{v}_z$] (b) Im[$\tilde{v}_z$]

FIG. 10: Normalised eigenfunction $\tilde{v}_z$ for the most unstable wall-mode at different Reynolds number. Panel (a) show the real part of the eigenfunction $\tilde{v}_z$ and Panel (b) show the imaginary part of the eigenfunction $\tilde{v}_z$ for $H = 7.77$, $k_{cr} = 0.92$ and Re as shown in figure.

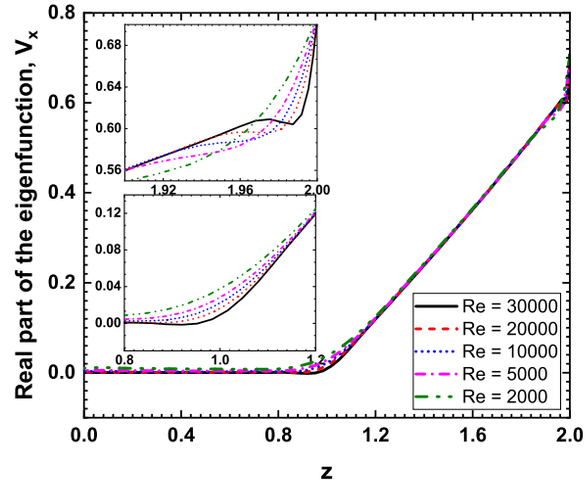

FIG. 11: Real part of the normalised eigenfunction $\tilde{v}_x$ for the inviscid mode: Data for $H = 7.77$, $k_{cr} = 0.56$ and Re as mentioned in the figure.

fluid in an unrestrained channel. This experimental observation further supports the numerical predictions in context to the effect of the unrestrained boundary condition. In figures 13 and 14, we present the variation of the real and imaginary parts of the eigenfunction $\tilde{v}_z$ with z for the inviscid mode at $H = 7.77$ and k_{cr}. We observe that there is no effect of solid layer-1 rigidly bonded to a solid substrate on the inviscid dynamics of the system. Also, there is no effect of the variation of the Reynolds number in most of the parameter space. The eigenfunctions $\tilde{v}_z$ merge for all Reynolds numbers near both the ends however, a little variation can be observed around the centerline (see inset in figure 13 and figure 14).

Thus by observing the variation of normal and tangential velocity fluctuations with z, we con-

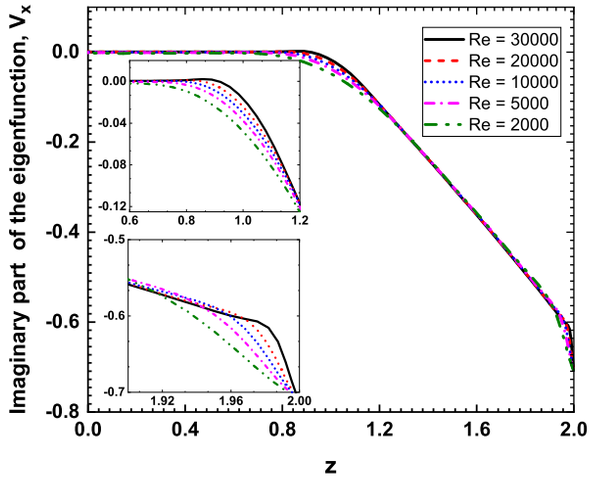

FIG. 12: Imaginary part of the normailsed eigenfunction $\tilde{v}_x$ for the inviscid mode: Data for $H = 7.77$, $k = 0.568$ and Re as mentioned in the figure.

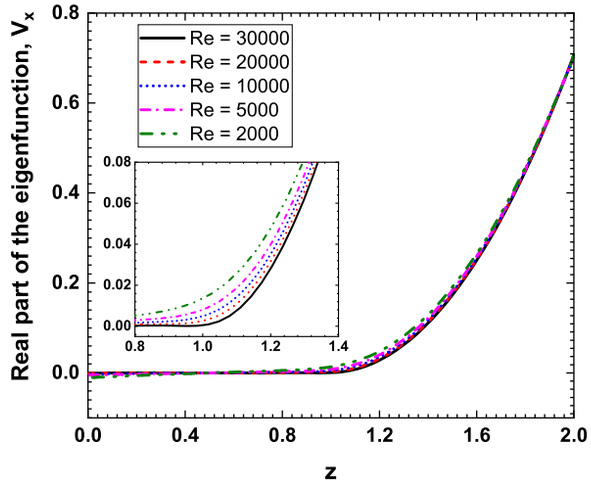

FIG. 13: Real part of the eigenfunction $\tilde{v}_z$ for the inviscid mode: Data for $H = 7.77$, $k = 0.56$ and Re as mentioned in the figure.

clude that the solid layer-1 has a minimal role in determining the stability of the most unstable modes (both wall and inviscid) of the system. To further verify this fact, we varied Γ values for solid layer-1 from 10^{-7} to 10^{7} (where $\Gamma \to 0$ for rigid solid) and the Γ values in the solid layer-2 are kept the same as required for the transition of flow from stable to unstable at $H = 7.77$ and $k = k_{cr}$. In figure 15, we present the neutral stability curves in the Re-Σ plane for both inviscid and wall modes for variation of Γ in lower solid layer, where we observe that the neutral stability curves for both the modes (wall and inviscid) overlap for all the cases of wide range of variation in the shear modulus in the solid layer-1. This confirms that the solid layer-1 does not affect the stability of the system and the dynamics of the system is driven by the presence of an unrestrained boundary.

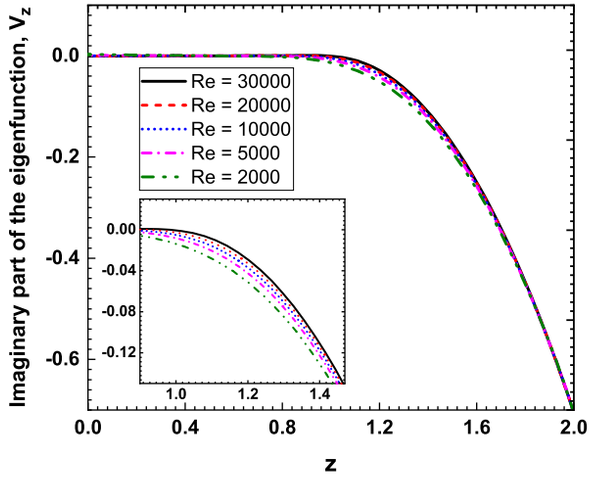

FIG. 14: Imaginary part of the eigenfunction $\tilde{v}_z$ for the inviscid mode: Data for $H = 7.77$, $k = 0.56$ and Re as mentioned in the figure.

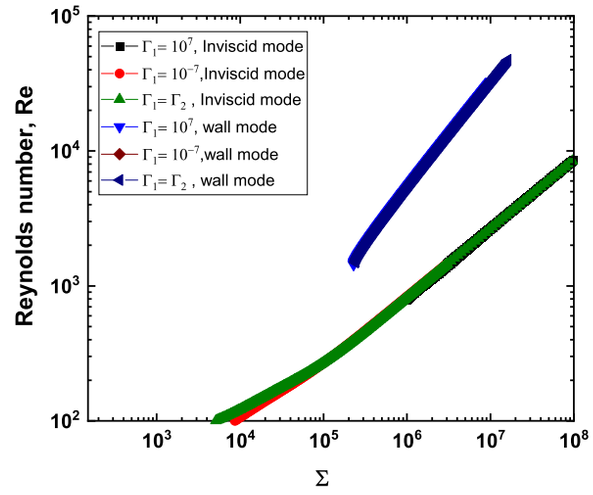

FIG. 15: Neutral stability curve in $Re - \Sigma$ plane: Data for $H = 7.77$, $k = 0.56$ for the inviscid mode and $k = 0.92$ for the wall mode and Γ as mentioned in the figure.

IV. CONCLUSIONS

We analysed the linear stability of the pressure-driven flow of a Newtonian fluid in a deformable channel with an unrestrained top boundary to understand its role on the stability of the system. The results suggest that, in the limit of high Reynolds number, both wall modes ($Re \sim \Sigma^{3/4}$) and inviscid modes ($Re \sim \Sigma^{1/2}$) are destabilised by the presence of the unrestrained boundary. The extent of destabilization is more pronounced when the ratio of solid to fluid thickness, $H \sim O(1)$, and is only moderate for $H \sim 8$. The eigenfunctions corresponding to the unstable wall and inviscid modes show an asymmetric behavior that is consistent with the experimental observations of

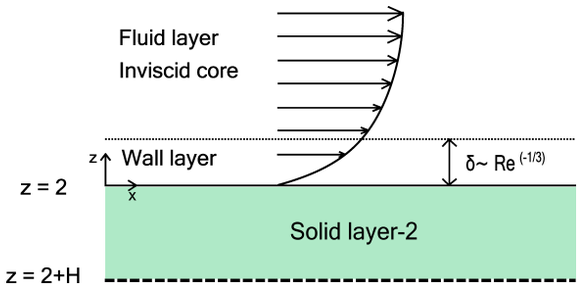

FIG. 16: Schematic diagram showing the flow structure for high Reynolds number wall modes in fluid flow through deformable channel. The unrestrained boundary at $z = H + 2$ is represented by dashed line.

Srinivas and Kumaran[45] for wall flutter transition. We also performed an asymptotic analysis for the wall mode instability, and the results are in good agreement with the numerical solution of the complete governing equations. We further showed that there is no effect of the lower solid layer on the critical Reynolds number and hence the stability of the system is only controlled by the thickness (H) and shear modulus (Γ) values of the top solid layer with the unrestrained boundary. Thus, in configurations containing a deformable wall with an unrestrained boundary, the flow stability is strongly influenced by the properties of solid layer with the unrestrained boundary, while the other solid layer has negligible effect on the same. This feature could be potentially exploited in manipulating and controlling flow instabilities in such systems.

Data Availability: The data that support the findings of this study are available from the corresponding author upon reasonable request.

Appendix: Asymptotic analysis of wall modes

In this appendix, we provide the details of the asymptotic analysis performed in the high Reynolds number limit[25,27] to estimate the wavespeed of "wall modes" for the pressure-driven flow of a Newtonian fluid in an unrestrained deformable channel to understand the influence of the "unrestrained boundary condition" on the dynamics of the system.

In this analysis, the flow velocity is divided into two distinct regions, as shown in figure 16. A "wall layer" is formed near the solid-fluid interface where the inertial and the viscous forces balance each other and an "inviscid core" develops in the central part of the fluid layer where the inertial forces dominate the viscous forces. Thus, the flow velocity field in the fluid layer is broadly divided as:

$$\tilde{v}_i = \tilde{v}_{inviscid,i} + \tilde{v}_{wall,i}\,, \tag{A.1}$$

where, i takes on the values x, z representing the directions in the Cartesian plane. We further divide the velocity field in the wall layer, $\tilde{v}_{wall,i}$ as:

$$\tilde{v}_{wall,i} = \tilde{v}_{top,wi} + \tilde{v}_{bot,wi}\,, \tag{A.2}$$

where, the subscripts top and bot represent the velocity field in the wall layer near the fluid-solid interfaces at $z = 2$ and $z = 0$ respectively. In this analysis, we focus on the wall layer near the fluid-solid interface at $z = 2$ to understand the influence of the unrestrained boundary condition at $z = H + 2$ on the stability of the system.

As the wavespeed of the wall modes is $O(Re^{-1/3})$ smaller in comparison to the characteristic velocity of the base flow,[25] $c/\Gamma \sim Re^{-1/3}$, within the present scheme of non-dimensionalisation. Also, the dimensionless maximum velocity of the base flow, $\Gamma \sim Re^{1/3}$, as $Re \sim \Sigma^{3/4}$ for the wall modes[25], where, $\Sigma = (\frac{Re}{\Gamma})^2$. Thus, we consider the wavespeed $c \sim O(1)$ and expand it in an asymptotic series as follows:

$$c = c^{(0)} + \delta c^{(1)} + \cdots \tag{A.3}$$

Here, $\delta \sim Re^{-1/3}$ is the thickness of the wall layer near the fluid-solid interface, and the relationship of the wall layer thickness with the Reynolds number is obtained by performing a scaling analysis on the x-momentum balance equation (Eq. 9) for the fluid. We now introduce an "inner-coordinate" ξ, for the wall layer near $z = 2$, such that $(2 - z) = \xi\delta$ and the derivatives d_z in the wall layer transform as $d_z = \delta^{-1} d_\xi$, where $d_\xi = d/d\xi$. The base-flow velocity profile (Eq. 1) is re-scaled in the wall layer as:

$$\bar{V}_x = \Gamma(2 - \xi\delta)\delta\xi, \tag{A.4}$$

where, $\Gamma = \Gamma_0 Re^{1/3}$ and Γ_0 is an $O(1)$ quantity. The dynamic quantities in the fluid layer are expanded in the asymptotic series as follows:

$$\tilde{v}_{\text{top},wx} = \tilde{v}^{(0)}_{\text{top},wx} + \delta\tilde{v}^{(1)}_{\text{top},wx} + \cdots \tag{A.5}$$

$$\tilde{v}_{\text{top},wz} = \delta\tilde{v}^{(0)}_{\text{top},wz} + \delta^2\tilde{v}^{(1)}_{\text{top},wz} + \cdots \tag{A.6}$$

$$\tilde{p}_{\text{top},wf} = \tilde{p}^{(0)}_{\text{top},wf} + \delta p^{(1)}_{\text{top},wf} + \cdots . \tag{A.7}$$

The above expansions (A.5-A.7) along with the scales for z-coordinate are substituted in the governing equations of the fluid flow (Eqs. 8-10), to obtain the following relations. The scaled continuity equation in the wall layer to the leading order in δ is given as:

$$-d_\xi\tilde{v}^{(0)}_{\text{top},wz} + ik\tilde{v}^{(0)}_{\text{top},wx} = 0 . \tag{A.8}$$

The scaled x-momentum balance equation is given as:

$$\mathrm{i}k\left[\delta\xi(2 - \xi\delta) - \frac{c^{(0)}}{\Gamma_0}\right]\tilde{v}^{(0)}_{\text{top},wx} + 2(\xi\delta - 1)\tilde{v}^{(0)}_{\text{top},wz} = -\mathrm{i}k\frac{\tilde{p}_{\text{top},wf}}{\Gamma_0} + \left(\mathrm{d}^2_\xi - (\Gamma_0\delta^2)k^2\right)\tilde{v}^{(0)}_{\text{top},wx} . \tag{A.9}$$

Thus, to a leading order in δ we obtain the following x-momentum equation:

$$\mathrm{i}k\left[2\xi - \frac{c^{(0)}}{\Gamma_0}\right]\tilde{v}^{(0)}_{\text{top},wx} - 2\tilde{v}^{(0)}_{\text{top},wz} = -\mathrm{i}k\frac{\tilde{p}^{(0)}_{\text{top},wf}}{\Gamma_0} + \mathrm{d}^2_\xi\tilde{v}^{(0)}_{\text{top},wx} . \tag{A.10}$$

Similarly, the scaled z-momentum balance equation is given as :

$$\mathrm{i}k\left[\delta\xi(2 - \xi\delta) - \frac{c^{(0)}}{\Gamma_0}\right]\tilde{v}^{(0)}_{\text{top},wz} = -\delta^{-2}\frac{\mathrm{d}_\xi\tilde{p}_{\text{top},wf}}{\Gamma_0} + \left(\mathrm{d}^2_\xi - (\Gamma_0\delta^2)k^2\right)\tilde{v}^{(0)}_{\text{top},wz} . \tag{A.11}$$

To a leading order in δ we obtain the following z-momentum equation:

$$\mathrm{d}_\xi\tilde{p}_{\text{top},wf} = 0 . \tag{A.12}$$

Equations (A.8), (A.10) and (A.12) are combined to obtain a fourth-order differential equation for $\tilde{v}^{(0)}_{\text{top},wz}$ to a leading order in δ:

$$\left[\mathrm{d}_\xi^2 - \mathrm{i}k\left(2\xi - \frac{c^{(0)}}{\Gamma_0}\right)\right]\mathrm{d}_\xi^2\tilde{v}^{(0)}_{\text{top},wz} = 0\,. \tag{A.13}$$

We further define another variable y, such that $y = (2\mathrm{i}k)^{1/3}\left[\xi - c^{(0)}/\left(2\Gamma_0\right)\right]$ and $\mathrm{d}_\xi = (2ik)^{(1/3)}d_y$. Thus, the equation A.13 takes the following form:

$$\left[\mathrm{d}_y^2 - y\right]\mathrm{d}_\xi^2\tilde{v}^{(0)}_{\text{top},wz} = 0\,. \tag{A.14}$$

The general solution to the equation A.14 is given as:

$$\tilde{v}^{(0)}_{\text{top},wz} = C_1 + C_2\xi + C_3[yAi(y,1) - Ai(y,-1)] + C_4[yBi(y,1) - Bi(y,-1)], \tag{A.15}$$

where, $Ai(y,p)$ and $Bi(y,p)$ are the generalized Airy functions ($p = \pm 1$)[25]. The Airy functions $Ai(y,p)$ are convergent in the limit $\xi \to \infty$ if $(-\pi/3) < \mathrm{Arg}(\xi) < (\pi/3)$. Hence, we choose $\mathrm{Arg}\left(\mathrm{i}^{1/3}\right) = \pi/6$ in the definition of y. The Airy function $Bi(y,p)$ diverges in this domain, so we are required to set $C_4 = 0$. Also, we set the coefficients C_1 and C_2 to be 0 as C_1 and $C_2\xi$ are the inviscid solutions[27]. The resulting velocity and pressure profiles in the wall layer are reduced to the following from:

$$\tilde{v}^{(0)}_{\text{top},wz} = C_3 2^{-1/3}(\mathrm{i}k)^{2/3}[yAi(y,1) - Ai(y,-1)]\,, \tag{A.16}$$

$$\tilde{v}^{(0)}_{\text{top},wx} = C_3 Ai(y,1)\,, \tag{A.17}$$

$$\tilde{p}^{(0)}_{\text{top},wf} = 0\,. \tag{A.18}$$

Now, to obtain the next dominant contribution in the fluid velocity field, $\tilde{v}_{inviscid,i}$, we set $Re^{-1} = 0$ in the linearised governing equations for the fluid flow (Eqs. 8-10) and expand the velocities and pressures for the "inviscid-layer" in the following asymptotic series:

$$\tilde{v}_{inviscid,z} = \delta\tilde{v}^{(0)}_{inviscid,z} + \delta^2\tilde{v}^{(1)}_{inviscid,z} + \cdots\,, \tag{A.19}$$

$$\tilde{v}_{inviscid,x} = \delta\tilde{v}^{(0)}_{inviscid,x} + \delta^2\tilde{v}^{(1)}_{inviscid,x} + \cdots\,, \tag{A.20}$$

$$\tilde{p}_{inviscid,f} = \tilde{p}^{(0)}_{inviscid,f} + \delta\tilde{p}^{(1)}_{inviscid,f} + \cdots\,. \tag{A.21}$$

These expansions are substituted in the governing equations for the inviscid-core layer which are further reduced to obtain a single second-order differential equation in the leading order of the small parameter δ:

$$\left(d_z^2 - k^2\right)\tilde{v}^{(0)}_{inviscid,z} + 2\tilde{v}^{(0)}_{inviscid,z} = 0. \tag{A.22}$$

The general solution to the differential equation A.22 is given as:

$$\tilde{v}^{(0)}_{inviscid,z} = C_1 e^{(\sqrt{k^2-2})z} + C_2 e^{-(\sqrt{k^2-2})z}. \tag{A.23}$$

The constants C_1 and C_2 can be obtained using the boundary conditions at the fluid-solid interfaces, and the expressions for $\tilde{v}^{(0)}_{inviscid,x}$ and $\tilde{p}^{(0)}_{inviscid,f}$ can be derived from the governing equations for the inviscid limit.

Next, we present the asymptotic expansions for wall displacement fields. We consider $\tilde{u}_x \sim O(1)$[25], that gives $\tilde{u}_z \sim O(1)$ in the bulk of the wall medium such that:

$$\tilde{u}_x = \tilde{u}_x^{(0)} + \delta\tilde{u}_x^{(1)} + \cdots , \tag{A.24}$$

$$\tilde{u}_z = \tilde{u}_z^{(0)} + \delta\tilde{u}_z^{(1)} + \cdots , \tag{A.25}$$

$$\tilde{p}_g = \tilde{p}_g^{(0)} + \delta\tilde{p}_g^{(1)} + \cdots . \tag{A.26}$$

The above expansions (Eqs. A.24-A.26) are substituted in the linearised governing equations (Eqs. 11-13) for the deformable solid-layer to obtain the following governing equations to the leading order in the small parameter δ:

$$\mathrm{d}_z\tilde{u}_z^{(0)} + \mathrm{i}k\tilde{u}_x^{(0)} = 0 , \tag{A.27}$$

$$-k^2\left(c^{(0)}\right)^2\tilde{u}_x^{(0)} = -\mathrm{i}k\tilde{p}_g^{(0)} + \left(\mathrm{d}_z^2 - k^2\right)\tilde{u}_x^{(0)} , \tag{A.28}$$

$$-k^2\left(c^{(0)}\right)^2\tilde{u}_z^{(0)} = -\mathrm{d}_z\tilde{p}_g^{(0)} + \left(\mathrm{d}_z^2 - k^2\right)\tilde{u}_z^{(0)} . \tag{A.29}$$

These equations (A.27 - A.29) are further combined to obtain a fourth order differential equation for $\tilde{u}_z^{(0)}$ to a leading order in δ:

$$\left(\mathrm{d}_z^2 - k^2\right)^2\tilde{u}_z^{(0)} - k^2\left(c^{(0)}\right)^2\left(\mathrm{d}_z^2 - k^2\right)\tilde{u}_z^{(0)} = 0 . \tag{A.30}$$

The solution to the leading order displacement field $\tilde{u}_z^{(0)}$ is given as:

$$\tilde{u}_z^{(0)} = B_1\exp[kz] + B_2\exp[\gamma z] + B_3\exp[-kz] + B_4\exp[-\gamma z] , \tag{A.31}$$

$$\tilde{u}_x^{(0)} = B_1 i\exp[kz] + B_2(i\gamma/k)\exp[\gamma z] - iB_3\exp[-kz] - (i\gamma/k)\exp[-\gamma z] . \tag{A.32}$$

where, $\gamma = k\sqrt{1-(c^{(0)})^2}$. The constants B_1, B_2, B_3 and B_4 are determined using the boundary conditions at $z = H + 2$ and $z = 2$. The first correction to the displacement field, obtained in a similar manner is given as:

$$\tilde{u}_z^{(1)} = B_2\left(-k^2c^{(0)}c^{(1)}z/\gamma\right)\exp[\gamma z] - B_4 i\left(-k^2c^{(0)}c^{(1)}z/\gamma\right)\exp[-\gamma z] , \tag{A.33}$$

$$\tilde{u}_x^{(1)} = B_2 i\left(-k^2c^{(0)}c^{(1)}(1+\gamma z)/(\gamma k)\right)\exp[\gamma z] + B_4 i\left(-k^2c^{(0)}c^{(1)}(-1+\gamma z)\right)\exp[-\gamma z] . \tag{A.34}$$

The asymptotic series expansions for the solid displacement fields and the pressure in the gel layer (Eqs. A.24 - A.26), the flow velocities and pressure in the wall layer (Eqs.A.5 - A.7) and the flow velocities and pressure in the inviscid layer (Eqs. A.19 - A.21) are substituted in the boundary conditions (Eqs. 20 - 23) at the fluid-solid interface, $z = 2$. The transformed continuity condition for normal velocity (Eq. 20) is given as:

$$\delta\left(\tilde{v}_{inviscid,z}^{(0)} + \tilde{v}_{top,wz}^{(0)}\right) = -\,\mathrm{i}k\left(c^{(0)} + \delta c^{(1)} + \cdots\right)\times\left(\tilde{u}_z^{(0)} + \delta\tilde{u}_z^{(1)} + \cdots\right) . \tag{A.35}$$

To a leading order in δ, equation A.35 becomes:

$$\tilde{u}_z^{(0)} = 0. \tag{A.36}$$

The first correction to the equation (A.35) is given as:

$$\left(\tilde{v}_{inviscid,z}^{(0)} + \tilde{v}_{top,wz}^{(0)}\right) = -\mathrm{i}k\left(c^{(0)}\tilde{u}_z^{(1)}\right) . \tag{A.37}$$

Similarly, the transformed tangential velocity continuity condition (Eq. 21), is as follows:

$$\tilde{v}^{(0)}_{top,wx} - 2\delta^{-1}\Gamma_0 \left(\tilde{u}^{(0)}_z + \delta\tilde{u}^{(1)}_z + \cdots\right) = -\mathrm{i}k \left(c^{(0)} + \delta c^{(1)} + \cdots\right)\left(\tilde{u}^{(0)}_x + \delta\tilde{u}^{(1)}_x + \cdots\right). \quad \text{(A.38)}$$

The above equation gives the following condition to a leading order in δ:

$$\tilde{u}^{(0)}_z = 0. \quad \text{(A.39)}$$

It is to note here that this equation is identical to the equation A.36 obtained as leading order equation from the normal velocity boundary condition. The first correction to the equation (A.38) is given as:

$$\tilde{v}^{(0)}_{top,wx} - 2\Gamma_0\tilde{u}^{(1)}_z = -\mathrm{i}kc^{(0)}\tilde{u}^{(0)}_x. \quad \text{(A.40)}$$

The tangential stress balance at the fluid solid interface (Eq. 22), transforms as:

$$\Gamma_0\delta\left(-\mathrm{d}_\xi\tilde{v}^{(0)}_{top,wx} + \delta^2\mathrm{i}k\tilde{v}^{(0)}_{top,wz}\right) = \left[\left(\mathrm{d}_z\tilde{u}^{(0)}_x + \mathrm{i}k\tilde{u}^{(0)}_z\right) + \delta\left(\mathrm{d}_z\tilde{u}^{(1)}_x + \mathrm{i}k\tilde{u}^{(1)}_z\right)\right]. \quad \text{(A.41)}$$

The leading order relation and the first correction to equation A.41 are given as:

$$\left(d_z\tilde{u}^{(0)}_x + ik\tilde{u}^{(0)}_z\right) = 0\,, \quad \text{(A.42)}$$

$$-\Gamma_0\left(d_\xi\tilde{v}^{(0)}_{\mathrm{top},wx}\right) = \left(d_z\tilde{u}^{(1)}_x + ik\tilde{u}^{(1)}_z\right). \quad \text{(A.43)}$$

The transformed boundary condition for the normal stress balance (Eq. 23) at the fluid solid interface $z = 2$ becomes:

$$-\left(\tilde{p}^{(0)}_{\mathrm{top},wf} + \delta\tilde{p}^{(1)}_{\mathrm{top},wf}\right) + 2\Gamma_0\delta^2\left(-\mathrm{d}_\xi\tilde{v}^{(0)}_{\mathrm{top},wz}\right) = -\left(\tilde{p}^{(0)}_g + \delta\tilde{p}^{(1)}_g\right) + 2\left(\mathrm{d}_z\tilde{u}^{(0)}_z + \delta\mathrm{d}_z\tilde{u}^{(1)}_z\right). \quad \text{(A.44)}$$

The above equation can further be separated into the leading order and first correction equations given as:

$$-\tilde{p}^{(0)}_f = -\tilde{p}^{(0)}_g + 2\mathrm{d}_z\tilde{u}^{(0)}_z\,, \quad \text{(A.45)}$$

$$-\tilde{p}^{(1)}_f = -\tilde{p}^{(1)}_g + 2\mathrm{d}_z\tilde{u}^{(1)}_z\,. \quad \text{(A.46)}$$

This completes the set of boundary conditions at the fluid-sold interface at $z = 2$. We now present the boundary conditions at the "unrestrained boundary", i.e., $z = H + 2$. The boundary condition for tangential stress balance (Eq. 24) at the interface transforms as:

$$\mathrm{d}_z\left(\tilde{u}^{(0)}_x + \delta\tilde{u}^{(1)}_x\right) + ik\left(\tilde{u}^{(0)}_z + \delta\tilde{u}^{(1)}_z\right) = 0\,. \quad \text{(A.47)}$$

The leading order and first correction equations to the above boundary condition are given as:

$$\mathrm{d}_z\tilde{u}^{(0)}_x + ik\tilde{u}^{(0)}_z = 0\,, \quad \text{(A.48)}$$

$$\mathrm{d}_z\tilde{u}^{(1)}_x + ik\tilde{u}^{(1)}_z = 0\,. \quad \text{(A.49)}$$

The boundary condition for normal stress balance (Eq. 25) at the interface $z = H + 2$ transforms as:

$$-\left(\tilde{p}^{(0)}_g + \delta\tilde{p}^{(1)}_g\right) + 2\left(\mathrm{d}_z\tilde{u}^{(0)}_z + \delta\mathrm{d}_z\tilde{u}^{(1)}_z\right) = 0\,. \quad \text{(A.50)}$$

The above equation can further be expressed as the leading order and first correction equations at the unrestrained boundary:

$$\tilde{p}_g^{(0)} + 2\mathrm{d}_z\tilde{u}_z^{(0)} = 0\,, \tag{A.51}$$

$$\tilde{p}_g^{(1)} + 2\mathrm{d}_z\tilde{u}_z^{(1)} = 0\,. \tag{A.52}$$

However, if we consider the "rigidly bonded" boundary condition at $z = H + 2$, we get the following equations as leading order and first corrections:

$$\tilde{u}_z^{(0)} = 0, \tilde{u}_x^{(0)} = 0\,, \tag{A.53}$$

$$\tilde{u}_z^{(1)} = 0, \tilde{u}_x^{(1)} = 0\,. \tag{A.54}$$

This completes the description of the boundary conditions for the system under consideration. As we can notice, the velocity fields in the wall layer do not appear to the leading order in the boundary conditions. Thus, the leading order wavespeed is obtained by using the boundary conditions A.36, A.42, A.48, and A.51. This system of equations is written in a matrix form as $\mathbf{MB} = \mathbf{0}$, where $\mathbf{B}$ is a vector of constants B_1, B_2, B_3, and B_4 occurring in the equation (A.31). We obtain a characteristic equation by setting $\mathrm{Det}[\mathbf{M}] = 0$. The leading order wavespeed ($c^{(0)}$) obtained from the characteristic equation has multiple solutions that are real and positive, indicating that the perturbations are stable in the leading order approximation. Thus, we proceed to calculate the first correction to the wavespeed, $c^{(1)}$, by determining the $O(\delta)$ correction to the characteristic equation, $\mathrm{Det}[\mathbf{M}] = 0$. The results obtained for the first correction to the wavespeed ($c^{(1)}$) are "complex numbers," and so we set $\mathrm{Im}\left[c^{(1)}\right] = 0$ to find the value of Γ_0 required to obtain the neutrally stable modes. It is to note here that for each of the multiple solutions obtained for $c^{(0)}$, we can obtain a first correction $c^{(1)}$, which can further be used to determine the multiple solutions for the scaled velocity Γ_0 required to obtain the neutrally stable modes. This suggests that there can be multiple unstable solutions in the limit of high Reynolds number.

REFERENCES

[1]M. O. Kramer, " Reader's Forum," J . Aero. Sci. **27**, 68 (1960).

[2]M. O. Kramer, "Boundary layer stabilization by distributed damping," J. Amer. Soc. Nav. Engrs. **72**, 25 - 33 (1960).

[3]T. B. Benjamin, "Effect of a flexible surface on boundary layer stability," J. Fluid Mech. **9**, 513 - 532 (1960).

[4]M. T. Landahl, "On the stability of a laminar incompressible boundary layer over a flexible surface," J. Fluid Mech. **13(4)**, 609 - 632 (1962).

[5]T. B. Benjamin, "The threefold classification for unstable disturbances in flexible surfaces bounding inviscid flows," J. Fluid Mech. **16**, 436 - 450 (1963).

[6]C. H. Green, and C. H. Ellen, "The stability of plane Poiseuille flow between flexible walls," J. Fluid Mech. **51**, 403 - 416 (1972).

[7]J. Lahav, N. Eliezer, and A. Silberberg, "Gel - walled cylindrical channels as models for microcirculation: Dynamics of flow," Biorheology **10**, 595 - 604 (1973).

[8]P. Krindel, and A. Silberberg, "Flow through gel-walled tubes," J. Colloid Interface Sci. **71**, 34 - 50 (1979).

[9]P. G. Drazin, and W. H. Reid, "*Hydrodynamic Stability*," Cambridge University Press (1981).

[10]P. W. Carpenter, and A. D. Garrad, "The hydrodynamic stability of flows over Kramer-type compliant surfaces. part 1. Tollmien-schlichting instabilities," J. Fluid Mech. **155**, 465 - 510 (1985).

[11]P. W. Carpenter, and A. D. Garrad, "The hydrodynamic stability of flows over Kramer-type compliant surfaces. part 2. flow induced surface instabilities," J. Fluid Mech. **170**, 199 - 232 (1986).

[12]L. Landau, and E. Lifshitz, "*Theory of Elasticity*," Pergamon, New York, (1989).

[13]J. M. Rotenberry, and P. G. Saffman, "Effect of compliant boundaries on the weakly nonlinear shear waves in a channel flow," SIAM J. Appl. Math. **50**, 361 - 394 (1990).

[14]V. Kumaran, G. H. Fredickson, and P. Pincus, "Flow induced instability of the interface between a fluid and a gel at low Reynolds number," J. Phys. Paris II **4**, 893 - 904 (1994).

[15]V. Kumaran, "Stability of the flow of a fluid through a flexible tube at high Reynolds number," J. Fluid Mech. **302**, 117 - 139 (1995).

[16]C. Davies, and P. W. Carpenter, "Instabilities in a plane channel flow between compliant walls," J. Fluid Mech. **352**, 205 - 243 (1997).

[17]L. Srivatsan, and V. Kumaran, "Stability of the interface between a fluid and gel," J. Phys. II.France **7**, 947 - 963 (1997).

[18]V. Shankar, and V. Kumaran, "Stability of non-parabolic flow in a flexible tube," J. Fluid Mech. **395**, 211 - 236 (1999).

[19]J. A. Weideman, and S. C. Reddy, "A MATLAB differentiation matrix suite," ACM Transactions on Mathematical Software (TOMS) **26(4)**, 465 - 519 (2000).

[20]V. Kumaran, and R. Muralikrishnan, "Spontaneous growth of fluctuations in the viscous flow of a fluid past a soft interface," Phys. Rev. Lett. **84**, 3310 (2000).

[21]V. Kumaran, "Classification of instabilities in the flow past flexible surfaces," Curr. Sci. **79(6)**, 766 - 773 (2000).

[22]V. Shankar, and V. Kumaran, "Stability of fluid flow in a flexible tube to non-axisymmetric disturbances," J. Fluid Mech. **408**, 291 - 314 (2000).

[23]J. P. Boyd, "*Chebyshev and Fourier Spectral Methods*," 2nd edn. New York: Dover (2001).

[24]P. J. Schmid, and D. S. Henningson, "*Stability and transition in shear flows*," New York: Springer (2001).

[25]V. Shankar, and V. Kumaran, "Asymptotic analysis of wall modes in a flexible tube revisited," Eur. Phys. J. B **19**, 607 - 622 (2001).

[26]J. C. McDonald, and G. M. Whitesides, "Poly(dimethylsiloxane) as a material for fabricating microfluidic devices," Acc. Chem. Res. **35**, 491 – 499 (2002).

[27]V. Shankar, and V. Kumaran, "Stability of wall modes in fluid flow past a flexible surface," Phys. Fluids **14**, 2324 - 2338 (2002).

[28]V. Gkanis, and S. Kumar, "Instability of creeping couette flow past a neo-hookean solid," Phys. Fluids **15**, 2864 - 2471 (2003).

[29]H. A. Stone, A. D. Stroock, and A. Ajdari, "Engineering flows in small devices: Microfluidics toward a Lab-on-a-Chip," Annu. Rev. Fluid Mech. **36**, 381 – 411 (2004).

[30]J. B. Grotberg, and O. E. Jensen, "Biofluid mechanics in flexible tubes," Annu. Rev. Fluid Mech. **36**, 121 - 47 (2004).

[31]V. Gkanis, and S. Kumar, "Stability of pressure-driven creeping flows in channels lined with a nonlinear elastic solid," J. Fluid Mech. **524**, 357 - 375 (2005).

[32]T. M. Squires, and S. R. Quake, "Micro-fluidics Fluid physics at the nanoliter scale," Rev. Mod. Phys. **77**, 977–1026 (2005).

[33]A. Shrivastava, E. L. Cussler, and S. Kumar, "Mass transfer enhancement due to a soft elastic boundary," Chem. Engg. Sci. **63**, 4302–4305 (2008).

[34]D. Huh, B. D. Matthews, A. Mammoto, M. Montoya-Zavala, H. Y. Hsin, and D. E. Ingber, "Reconstituting organ-level lung functions on a chip", Science **328**, 1662–1668 (2010).

[35]Gaurav, and V. Shankar, "Stability of pressure-driven flow in a deformable neo-Hookean channel," J. Fluid Mech. **659**, 318 - 350 (2010).

[36]J. B. Grotberg, "Respiratory fluid mechanics," Phys. Fluids **23**, 021301 (2011).

[37]M. K. S. Verma, and V. Kumaran, "A dynamical instability due to fluid–wall coupling lowers the transition Reynolds number in the flow through a flexible tube," J. Fluid Mech. **705**, 322 - 347 (2012).

[38]M. K. S. Verma, and V. Kumaran, "A multifold reduction in the transition Reynolds number, and ultra-fast mixing, in a micro-channel due to a dynamical instability induced by a soft wall," J. Fluid Mech. **727**, 407 - 455 (2013).

[39]M. K. S. Verma, and V. Kumaran, "Stability of the flow in a soft tube deformed due to an applied pressure gradient," Phys. Rev. E **91(4)**, 043001 (2015).

[40]S. Srinivas, and V. Kumaran, "After transition in a soft-walled microchannel," J. Fluid Mech. **780**, 649-686 (2015).

[41]V. Kumaran, "Experimental studies on the flow through soft tubes and channels," Sadhana **40(3)**, 911 - 923 (2015).

[42]V. Shankar, "Stability of fluid flow through deformable tubes and channels: an overview," Sadhana **40(3)**, 925 - 943 (2015).

[43]V. Kumaran, and P. Bandaru, "Ultra-fast microfluidic mixing by soft-wall turbulence," Chem. Engg. Sci. **149**, 156 - 168 (2016).

[44]R. Patne, D. Giribabu, and V. Shankar, "Consistent formulations for stability of fluid flow through deformable channels and tubes," J. Fluid Mech. **827**, 31 - 66 (2017).

[45]S. S. Srinivas, and V. Kumaran, "Transitions to different kinds of turbulence in a channel with soft walls," J. Fluid Mech. **822**, 267 - 306 (2017).

[46]Y. Matia, T. Elimelech, and A. D. Gat, "Leveraging internal viscous flow to extend the capabilities of beam-shaped soft robotic actuators", Soft Robotics, **4**, 126–134 (2017).

[47]R. Patne, and V. Shankar, "Stability of flow through deformable channels and tubes: Implications of consistent formulation," J. Fluid Mech. **860**, 837 - 885 (2019).

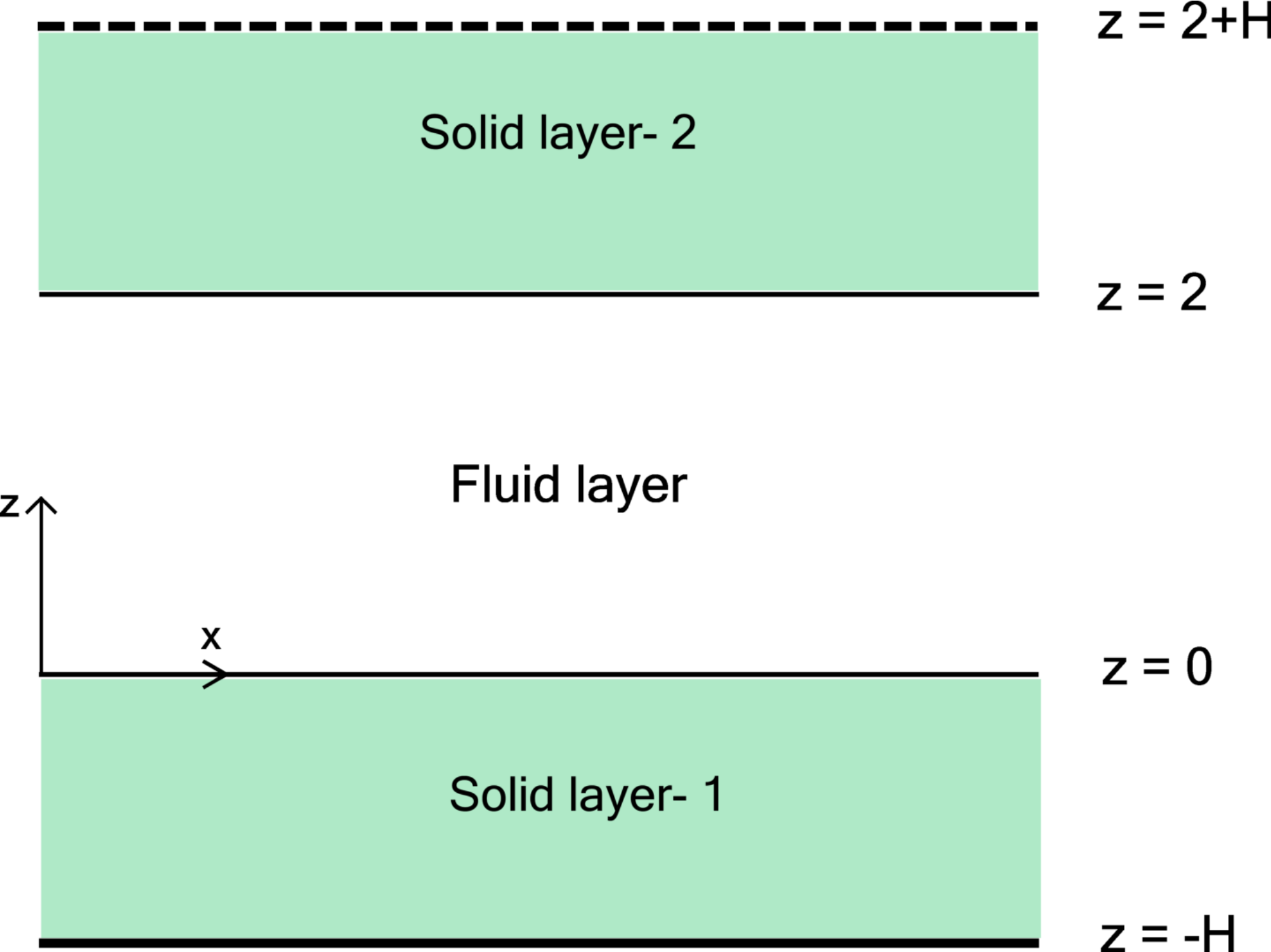
z = 2+H
Solid layer- 2
z = 2
Fluid layer
z
x
z = 0
Solid layer- 1
z = -H

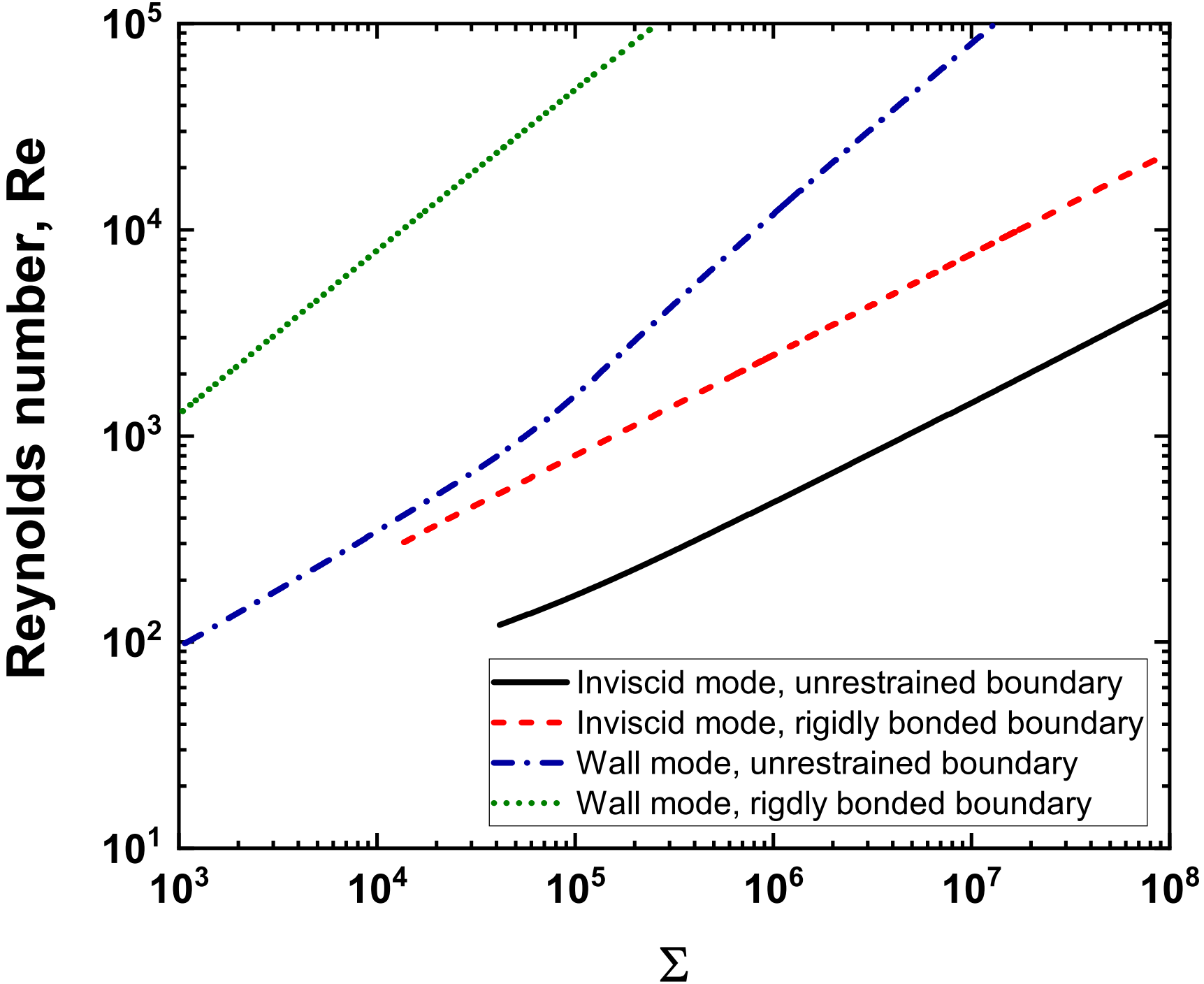
Reynolds number, Re
10^5
10^4
10^3
10^2
10^1
10^3
10^4
10^5
10^6
10^7
10^8
Σ
Inviscid mode, unrestrained boundary
Inviscid mode, rigidly bonded boundary
Wall mode, unrestrained boundary
Wall mode, rigdly bonded boundary

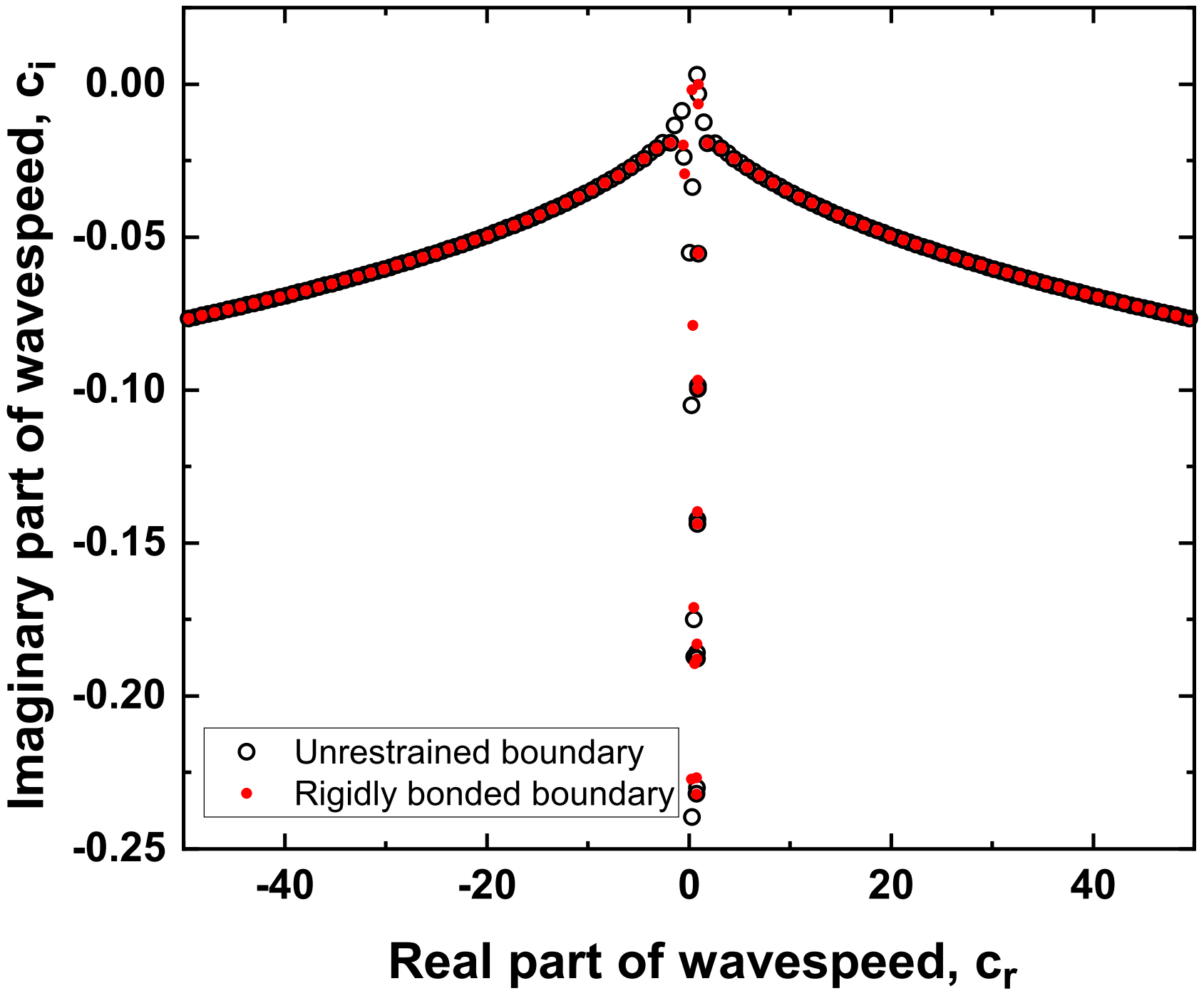
0.00
-0.05
-0.10
-0.15
-0.20
-0.25
Imaginary part of wavespeed, c_i
-40
-20
0
20
40
Real part of wavespeed, c_r
Unrestrained boundary
Rigidly bonded boundary

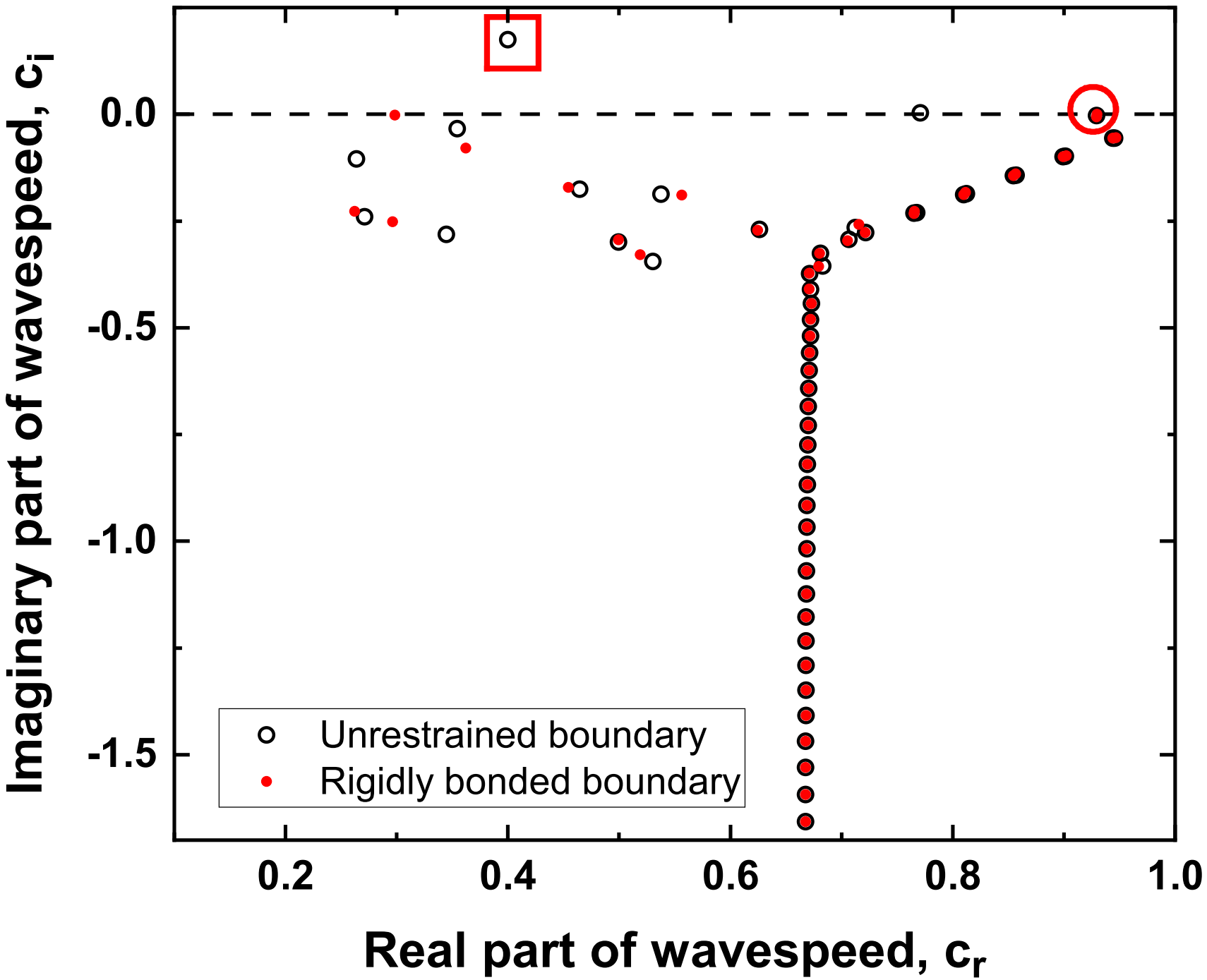
0.0
-0.5
-1.0
-1.5
0.2
0.4
0.6
0.8
1.0
Imaginary part of wavespeed, c_i
Real part of wavespeed, c_r
Unrestrained boundary
Rigidly bonded boundary

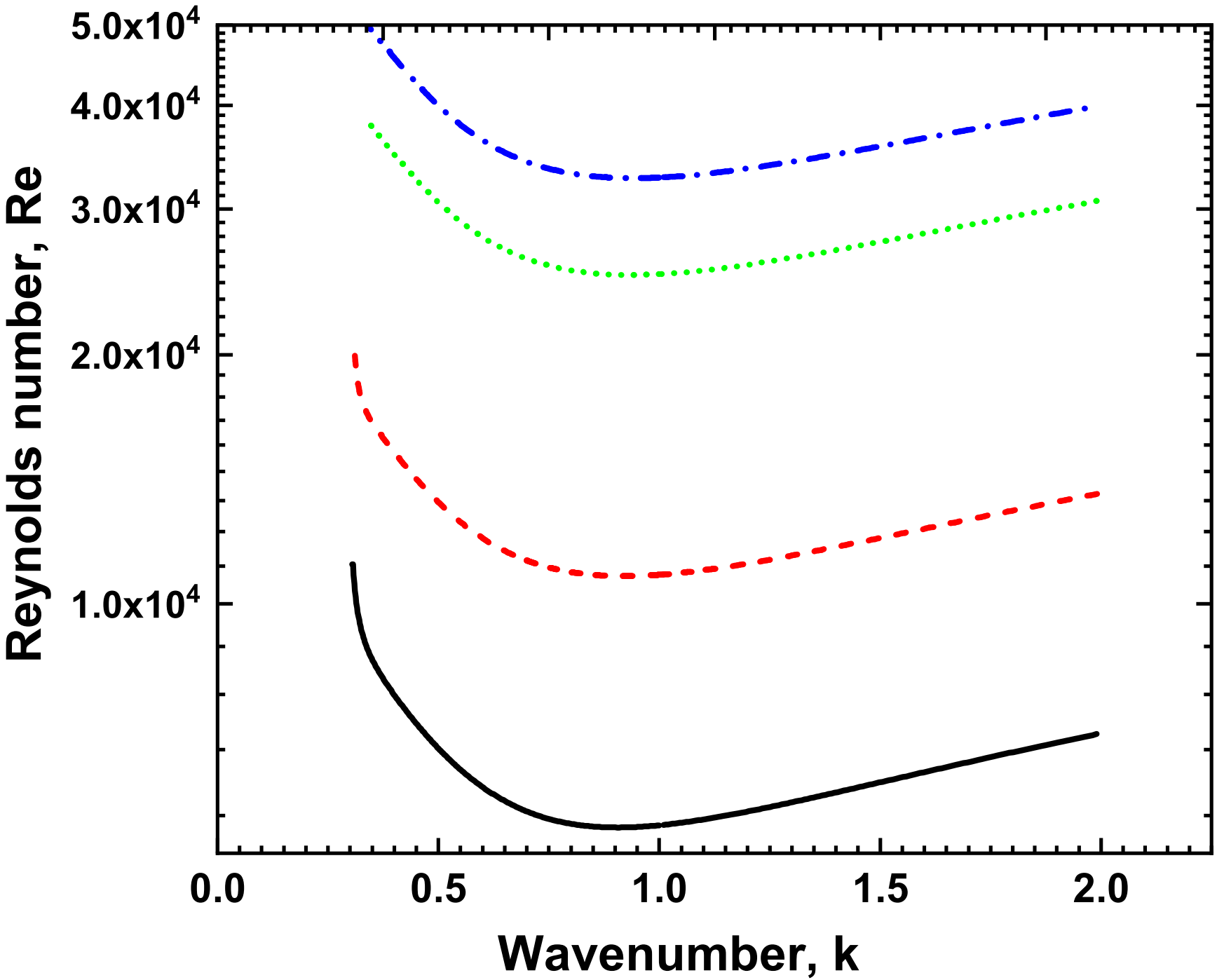
5.0x10^4
4.0x10^4
3.0x10^4
2.0x10^4
1.0x10^4
Reynolds number, Re
0.0
0.5
1.0
1.5
2.0
Wavenumber, k

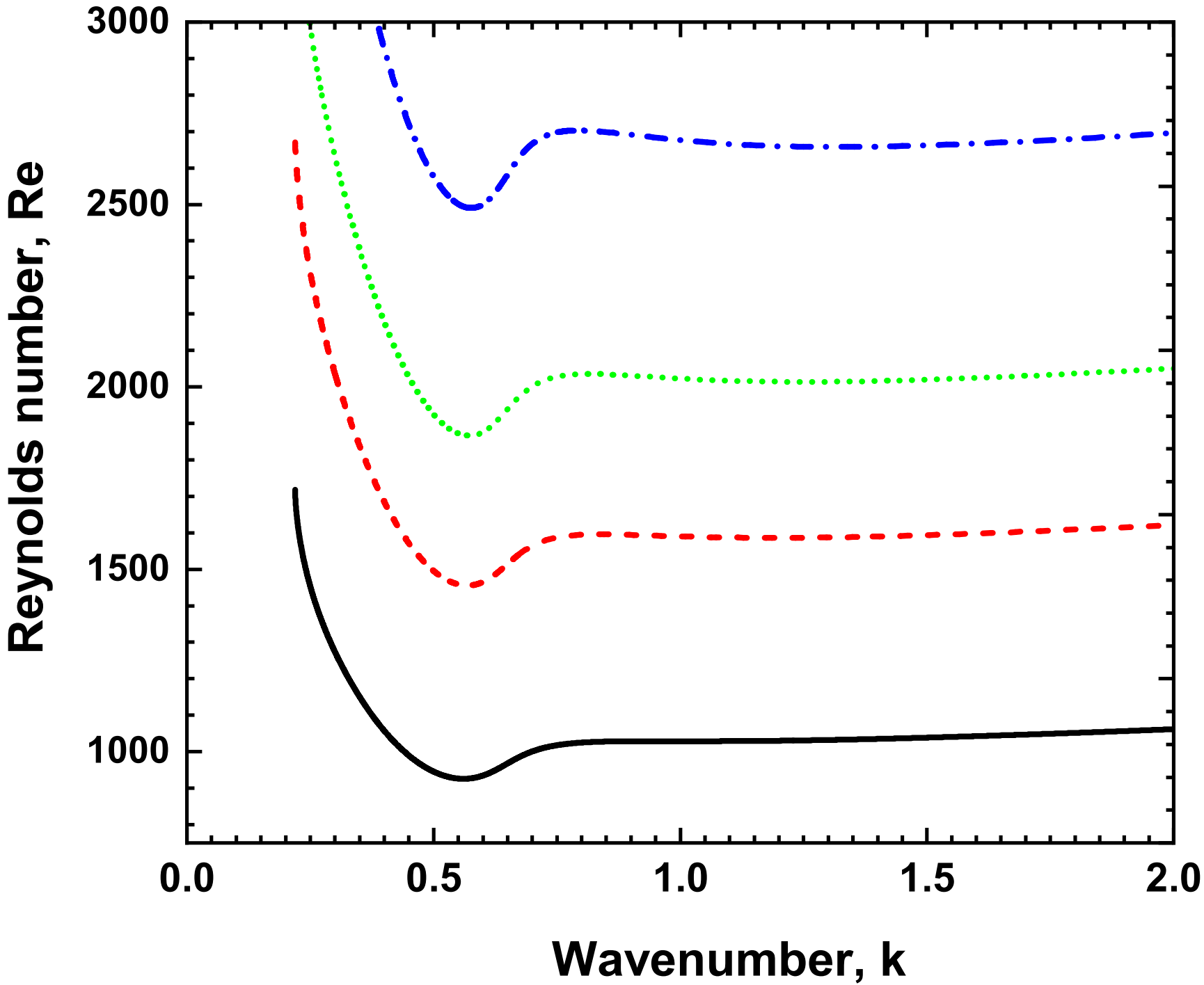
3000
2500
2000
1500
1000
Reynolds number, Re
0.0
0.5
1.0
1.5
2.0
Wavenumber, k

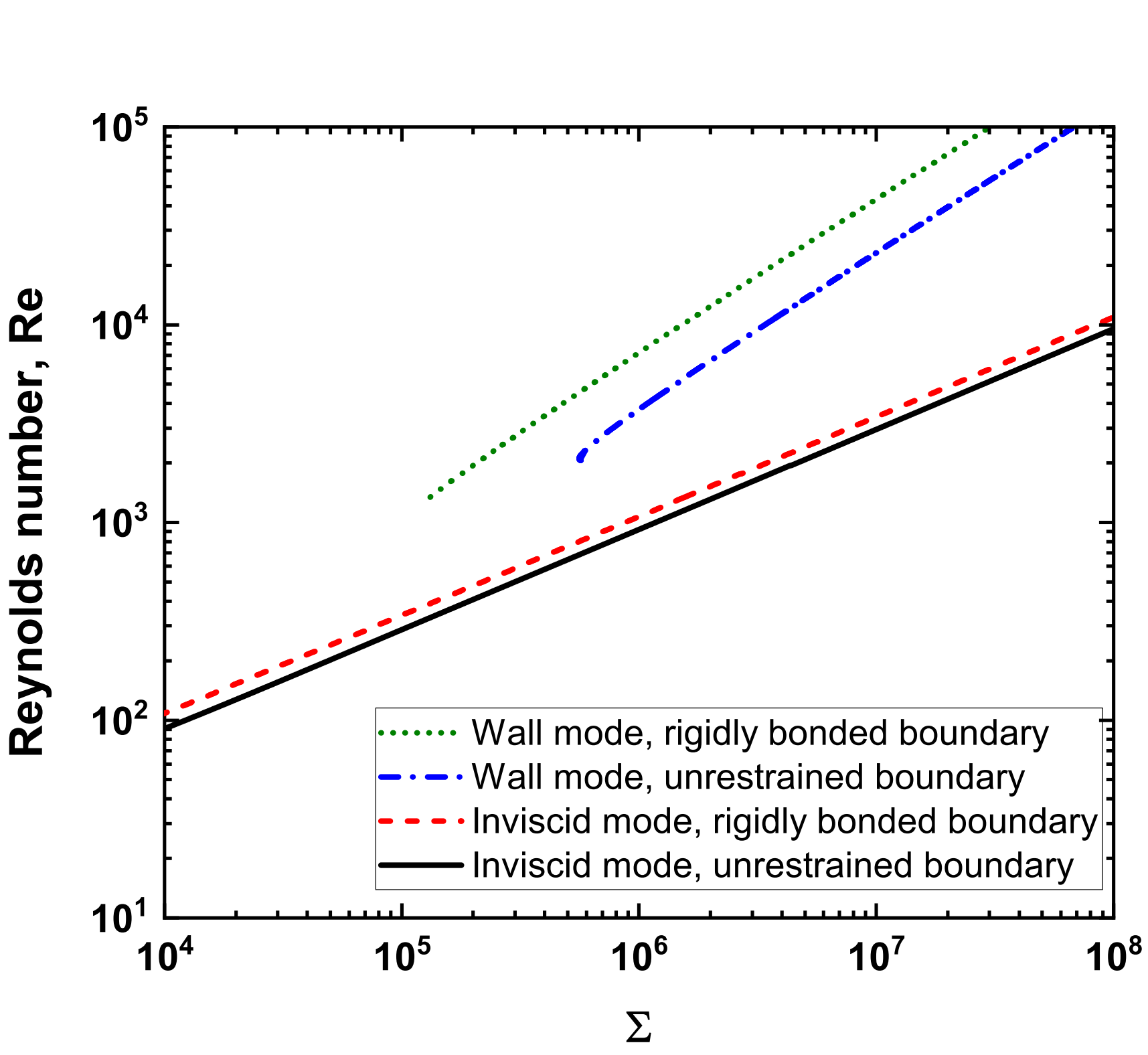
Reynolds number, Re
10^5
10^4
10^3
10^2
10^1
10^4
10^5
10^6
10^7
10^8
Σ
Wall mode, rigidly bonded boundary
Wall mode, unrestrained boundary
Inviscid mode, rigidly bonded boundary
Inviscid mode, unrestrained boundary

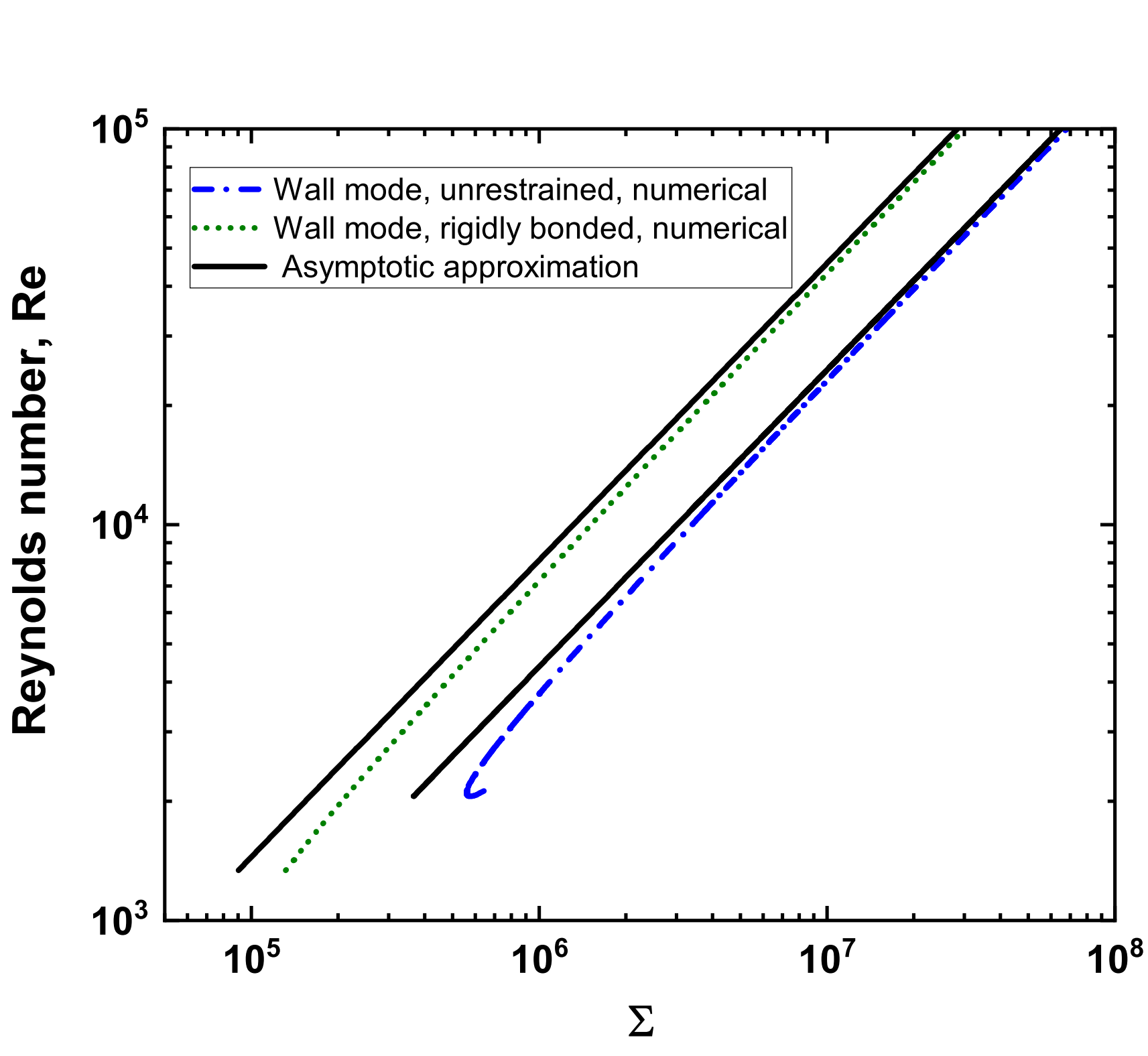
Wall mode, unrestrained, numerical
Wall mode, rigidly bonded, numerical
Asymptotic approximation
Reynolds number, Re
10^5
10^4
10^3
10^5
10^6
10^7
10^8
Σ

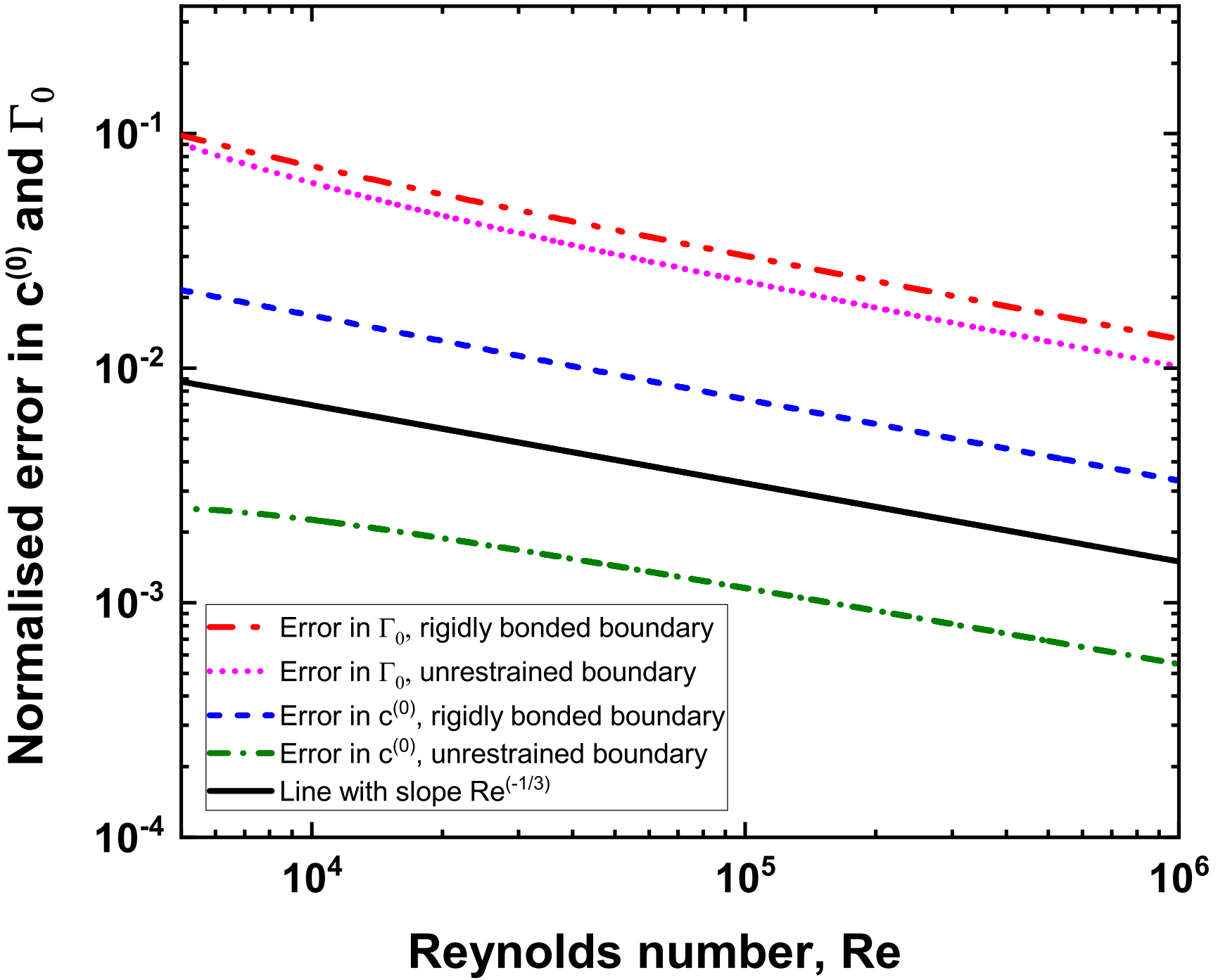
Normalised error in $c^{(0)}$ and Γ_0
10^{-1}
10^{-2}
10^{-3}
10^{-4}
10^4
10^5
10^6
Reynolds number, Re
Error in Γ_0, rigidly bonded boundary
Error in Γ_0, unrestrained boundary
Error in $c^{(0)}$, rigidly bonded boundary
Error in $c^{(0)}$, unrestrained boundary
Line with slope $Re^{(-1/3)}$

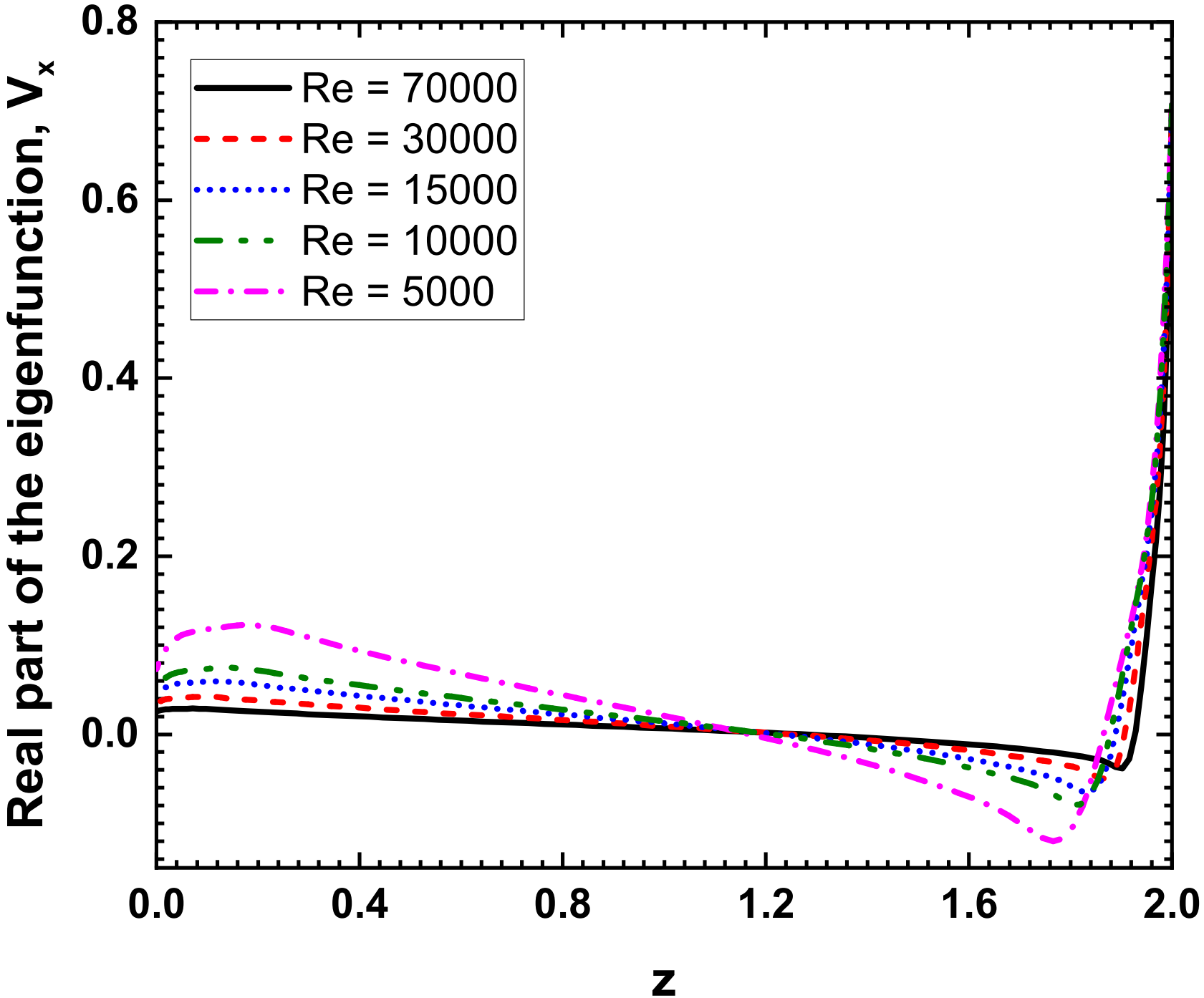
Re = 70000
Re = 30000
Re = 15000
Re = 10000
Re = 5000
Real part of the eigenfunction, V_x
z
0.0
0.2
0.4
0.6
0.8
0.0
0.4
0.8
1.2
1.6
2.0

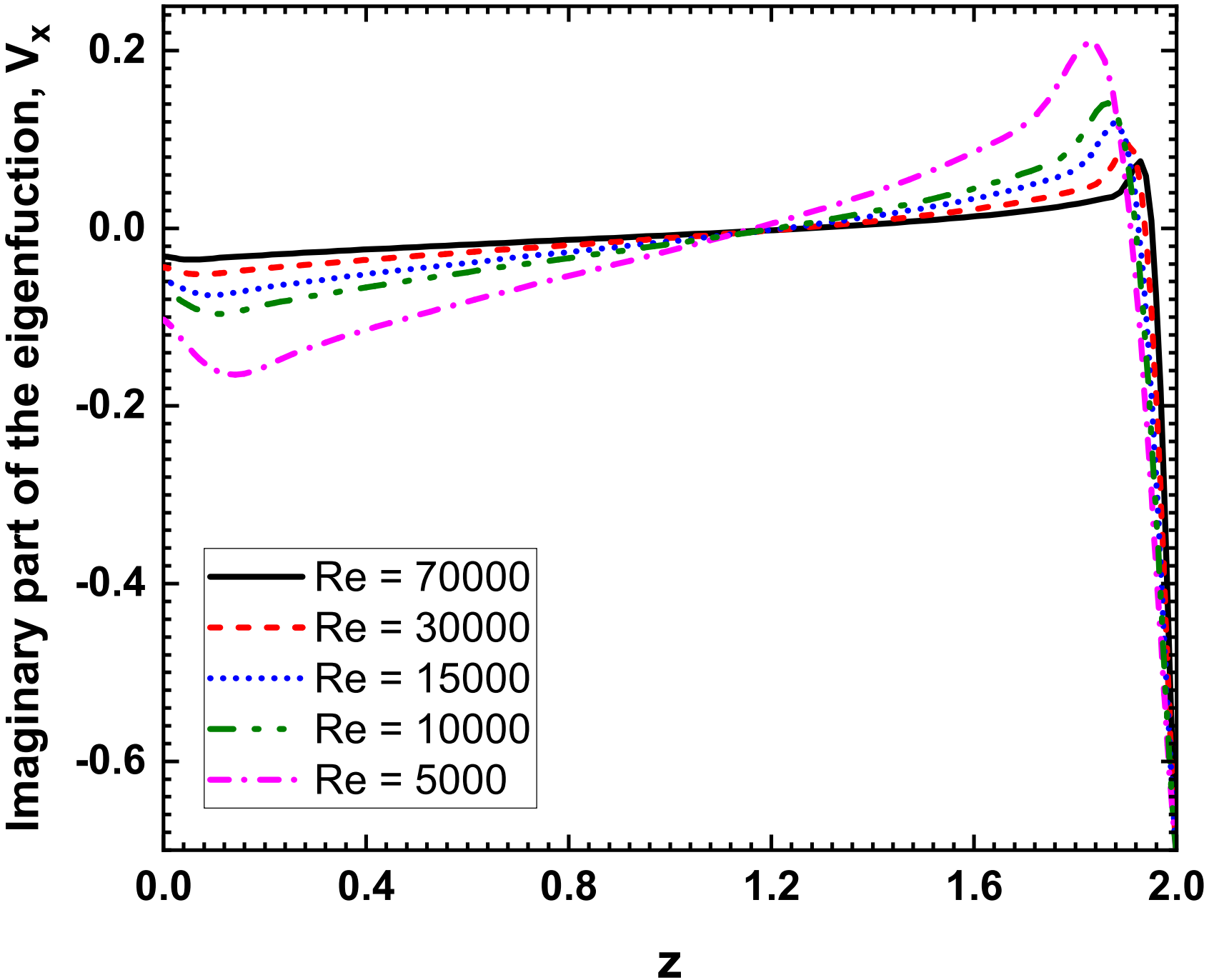
Imaginary part of the eigenfuction, V_x
0.2
0.0
-0.2
-0.4
-0.6
0.0
0.4
0.8
1.2
1.6
2.0
z
Re = 70000
Re = 30000
Re = 15000
Re = 10000
Re = 5000

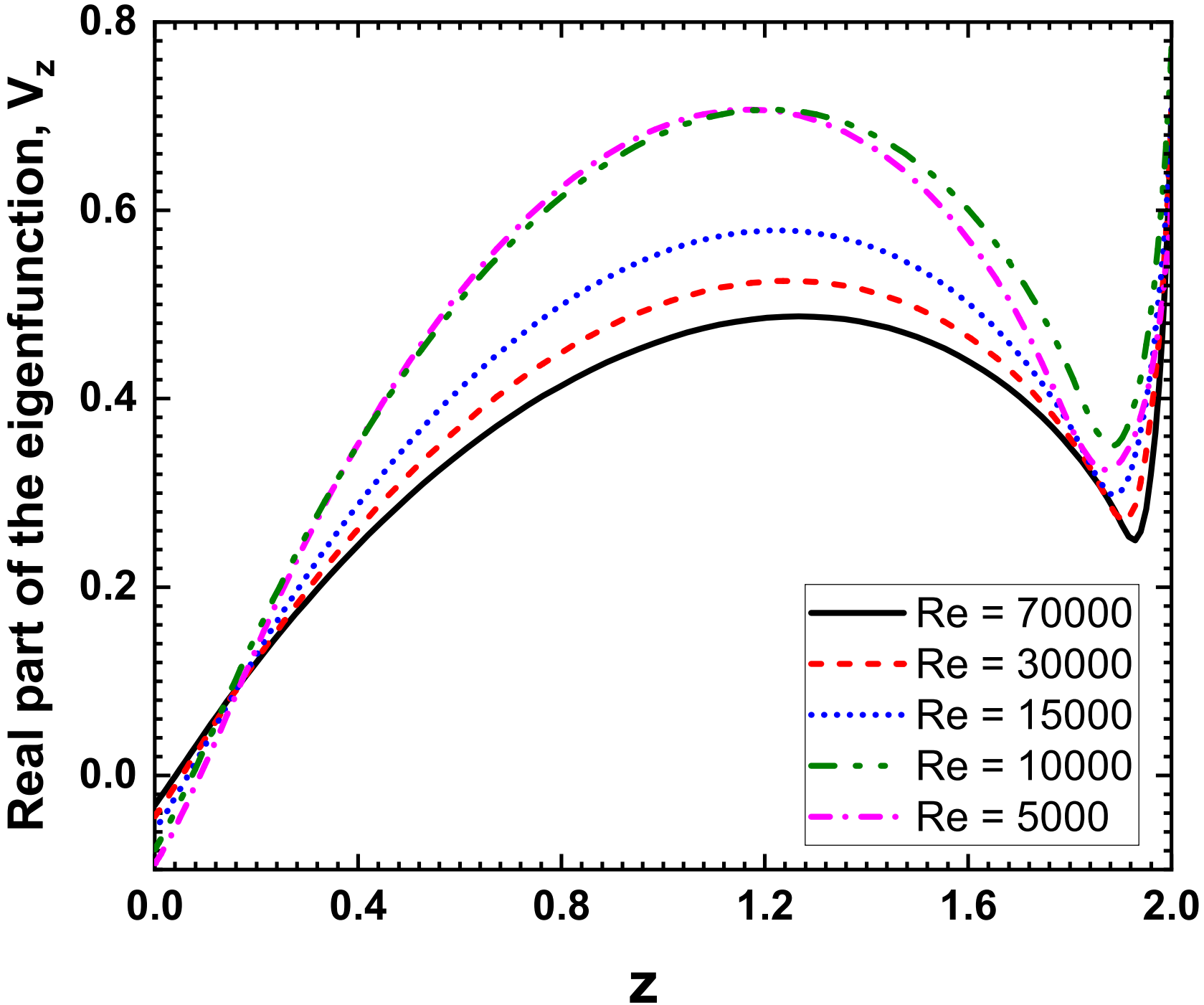
Real part of the eigenfunction, V_z
z
0.0
0.2
0.4
0.6
0.8
0.0
0.4
0.8
1.2
1.6
2.0
Re = 70000
Re = 30000
Re = 15000
Re = 10000
Re = 5000

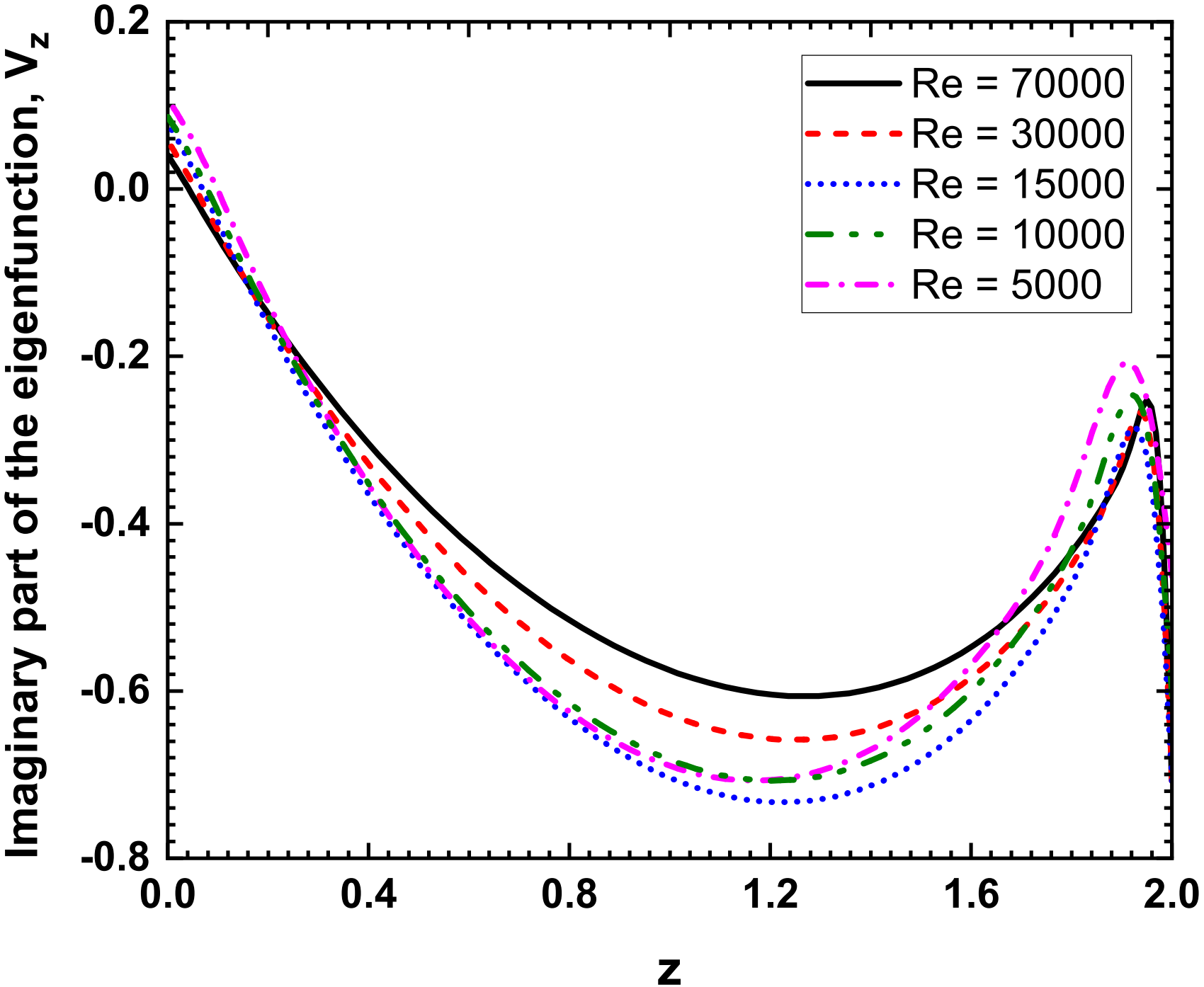
Imaginary part of the eigenfunction, V_z
z
0.2
0.0
-0.2
-0.4
-0.6
-0.8
0.0
0.4
0.8
1.2
1.6
2.0
Re = 70000
Re = 30000
Re = 15000
Re = 10000
Re = 5000

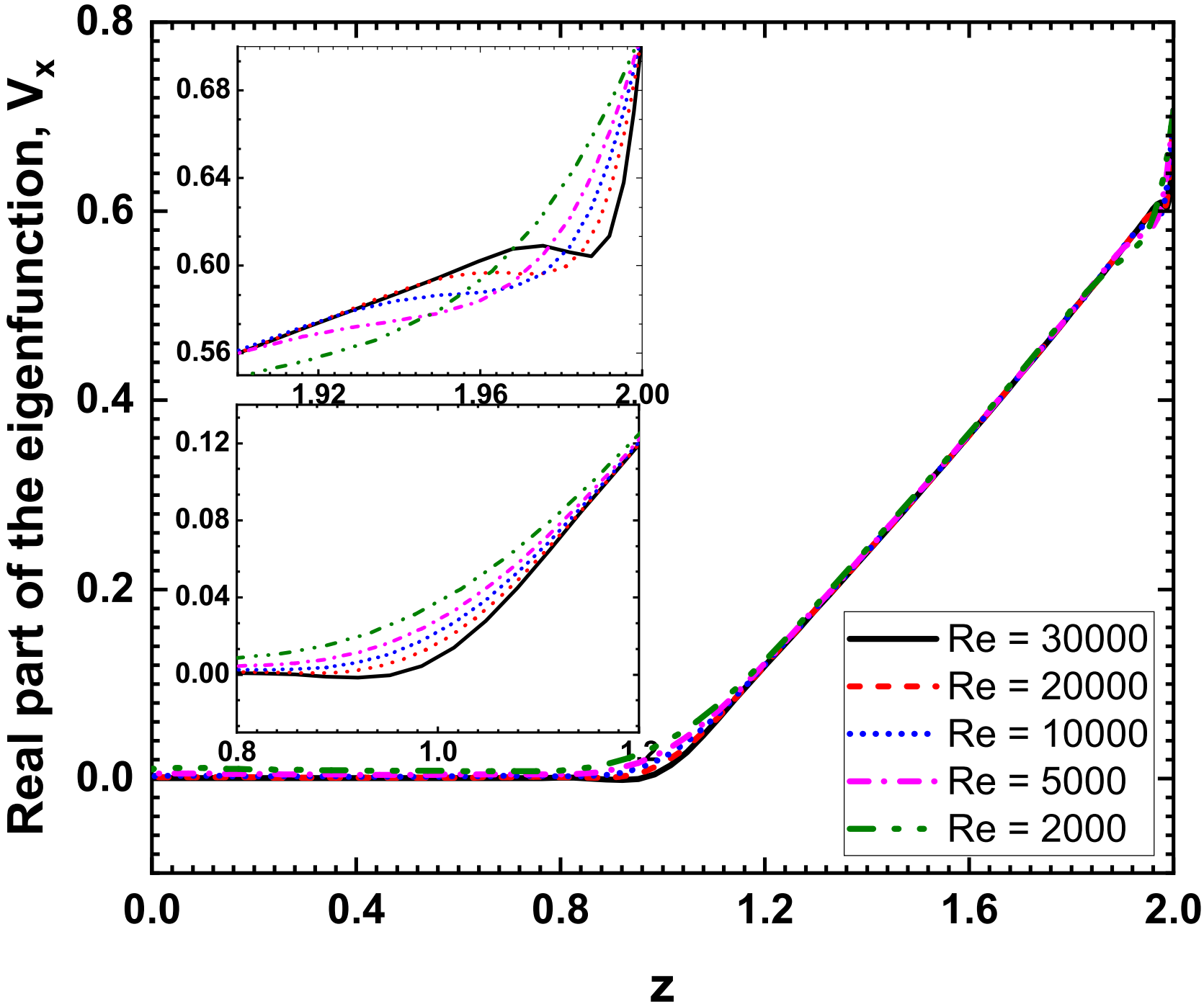
Real part of the eigenfunction, V_x
z
0.0
0.4
0.8
1.2
1.6
2.0
0.0
0.2
0.4
0.6
0.8
0.56
0.60
0.64
0.68
1.92
1.96
2.00
0.00
0.04
0.08
0.12
0.8
1.0
1.2
Re = 30000
Re = 20000
Re = 10000
Re = 5000
Re = 2000

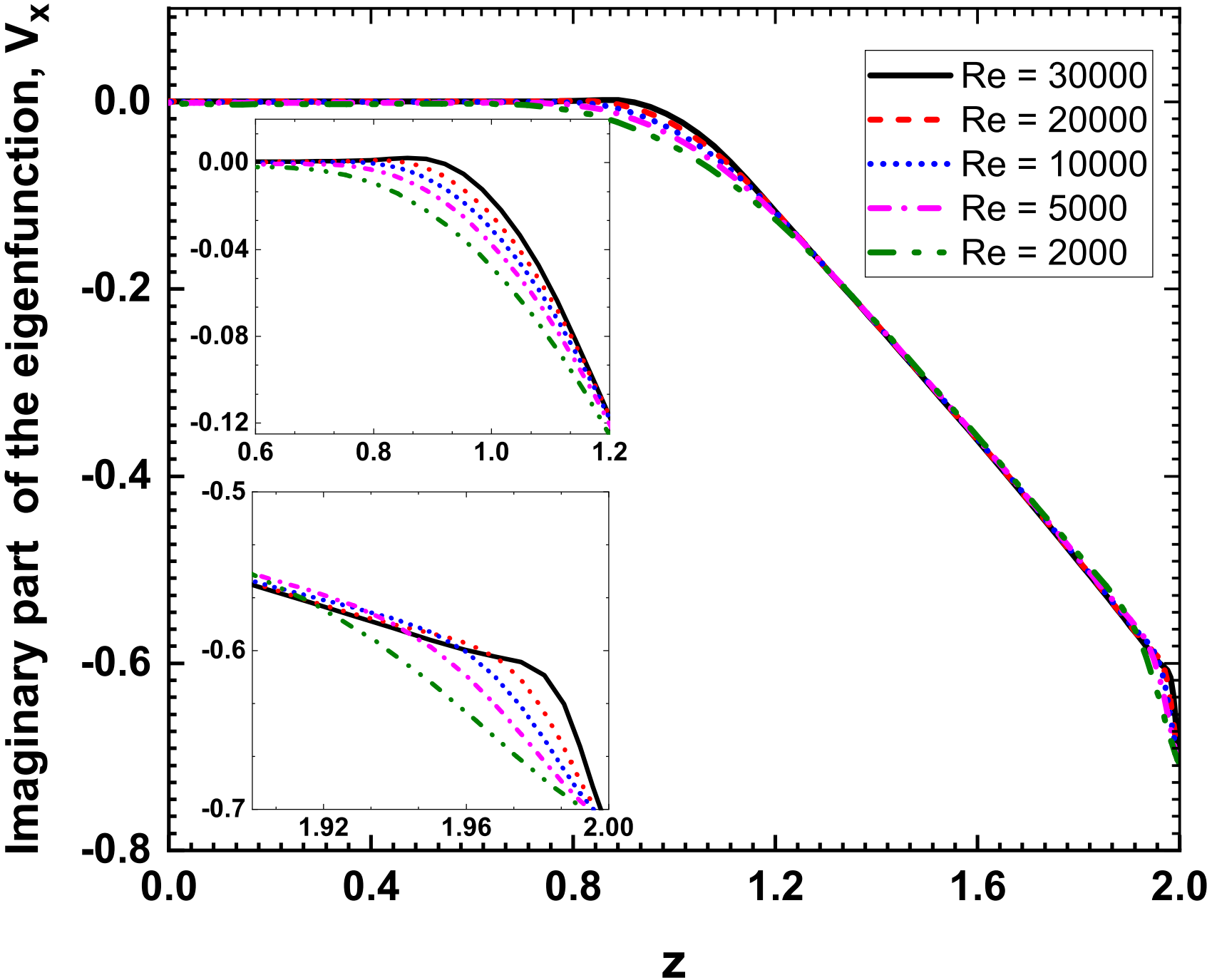
Imaginary part of the eigenfunction, V_x
z
Re = 30000
Re = 20000
Re = 10000
Re = 5000
Re = 2000
0.0
-0.2
-0.4
-0.6
-0.8
0.4
0.8
1.2
1.6
2.0
0.00
-0.04
-0.08
-0.12
0.6
1.0
1.2
-0.5
-0.6
-0.7
1.92
1.96
2.00

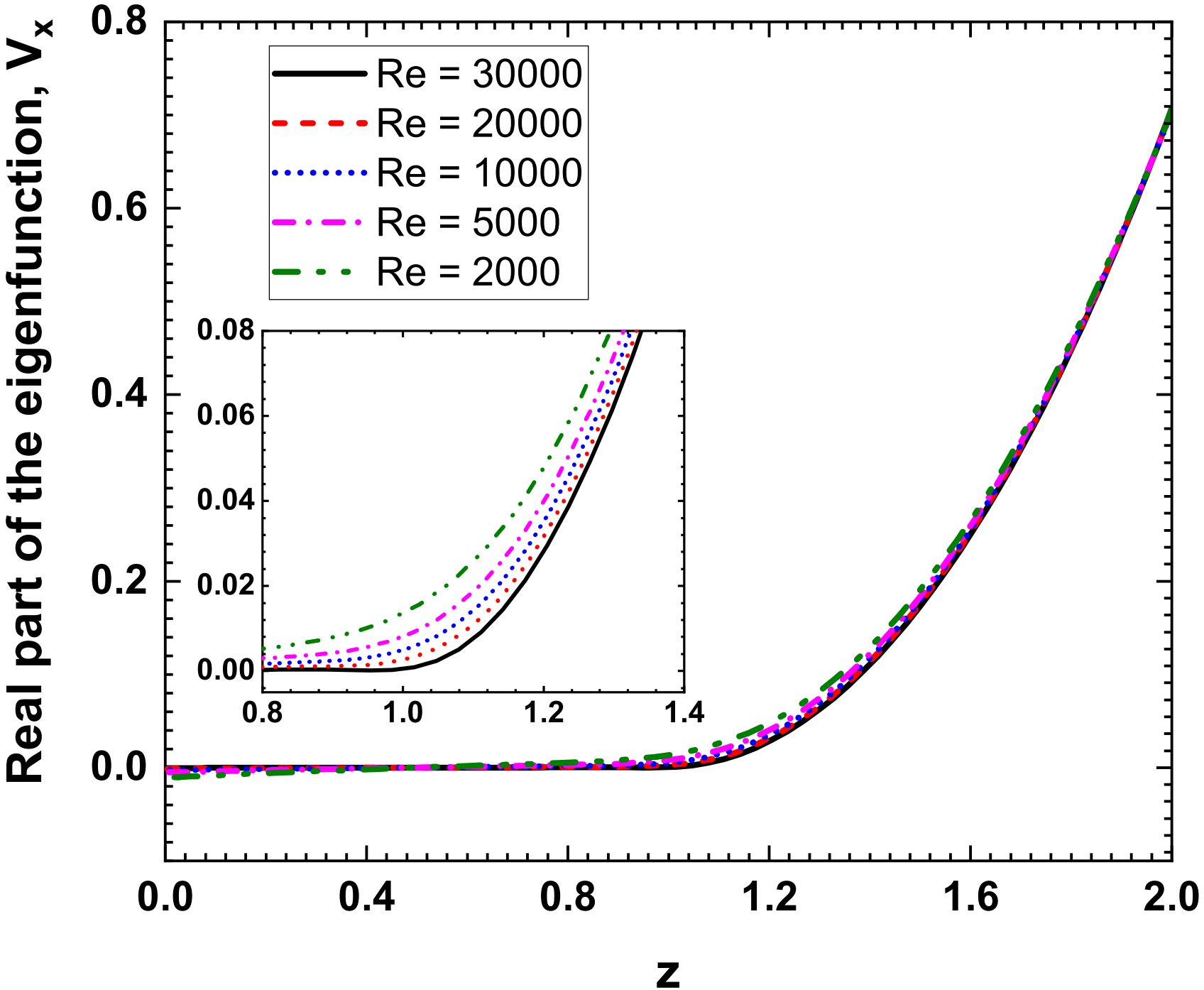
Re = 30000
Re = 20000
Re = 10000
Re = 5000
Re = 2000
Real part of the eigenfunction, V_x
z
0.0
0.2
0.4
0.6
0.8
0.0
0.4
0.8
1.2
1.6
2.0
0.00
0.02
0.04
0.06
0.08
0.8
1.0
1.2
1.4

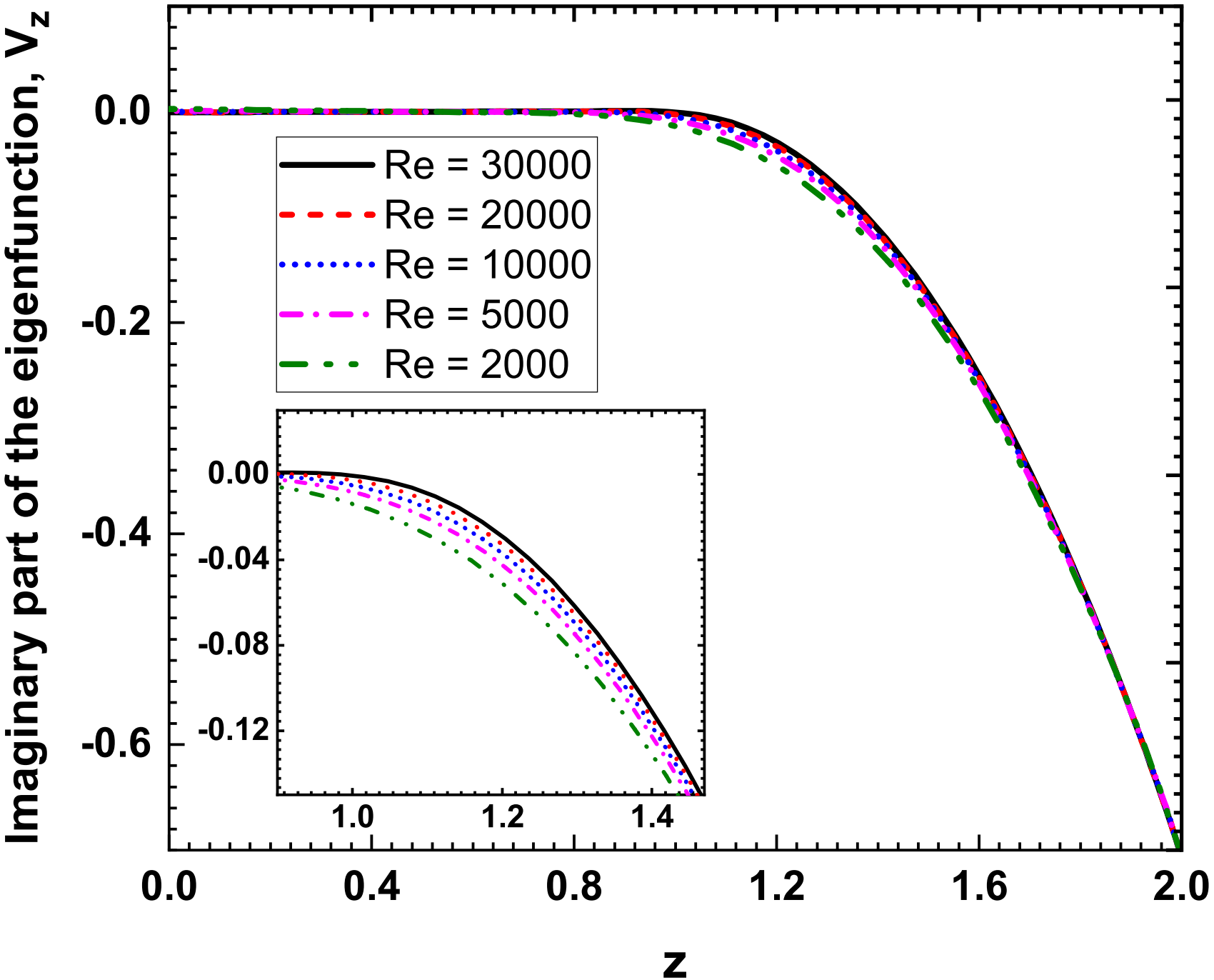
Imaginary part of the eigenfunction, V_z
z
0.0
-0.2
-0.4
-0.6
0.0
0.4
0.8
1.2
1.6
2.0
Re = 30000
Re = 20000
Re = 10000
Re = 5000
Re = 2000
0.00
-0.04
-0.08
-0.12
1.0
1.2
1.4

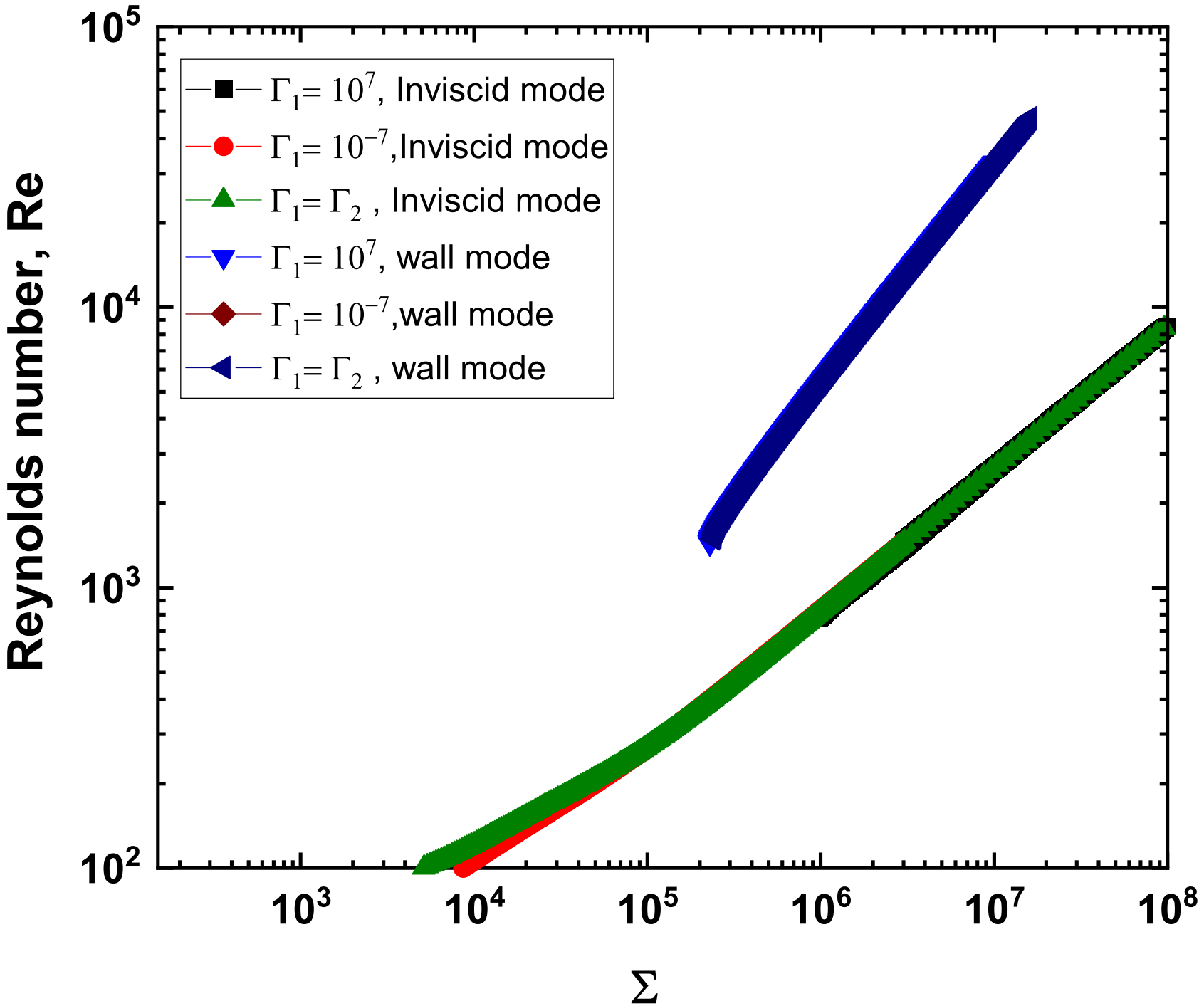
Reynolds number, Re
10^5
10^4
10^3
10^2
10^3
10^4
10^5
10^6
10^7
10^8
Σ
$\Gamma_1 = 10^7$, Inviscid mode
$\Gamma_1 = 10^{-7}$,Inviscid mode
$\Gamma_1 = \Gamma_2$, Inviscid mode
$\Gamma_1 = 10^7$, wall mode
$\Gamma_1 = 10^{-7}$,wall mode
$\Gamma_1 = \Gamma_2$, wall mode

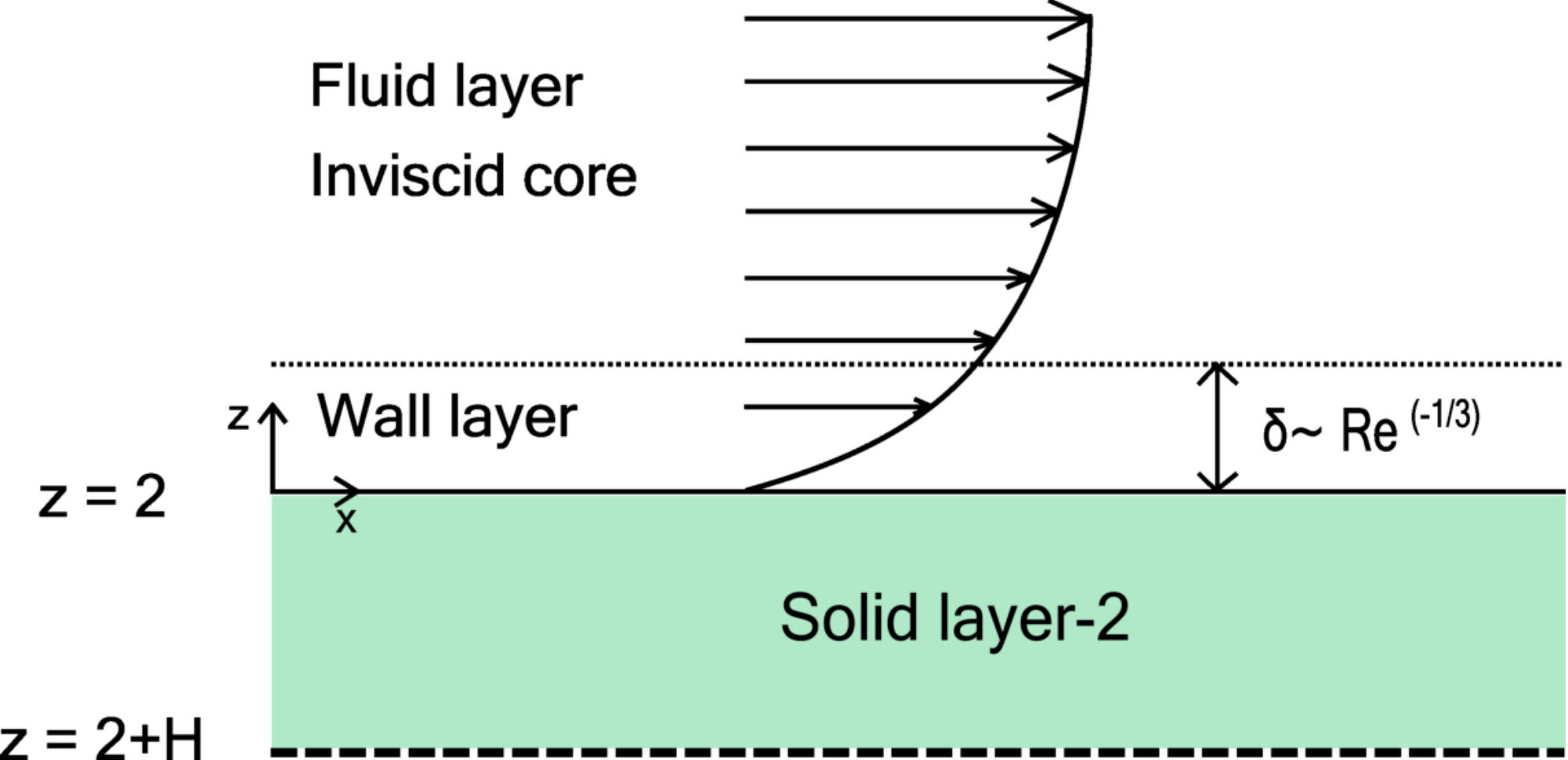
Fluid layer
Inviscid core
z
Wall layer
x
δ~ Re (-1/3)
z = 2
Solid layer-2
z = 2+H